Computers and Structures 321 (2026) 108094

Contents lists available at ScienceDirect

Computers and Structures

journal homepage: www.elsevier.com/locate/cas

Cyclic constitutive model for masonry joint damage and energy dissipation using the distinct element method

Yopi P. Oktiovan[a,*], Francesco Messali[a], Bora Pulatsu[b], Satyadhrik Sharma[c], José V. Lemos[d], Jan G. Rots[a]

[a] Faculty of Civil Engineering & Geosciences, Delft University of Technology, Stevinweg 1, 2628CN, Delft, the Netherlands
[b] Department of Civil and Environmental Engineering, Carleton University, Ottawa, Canada
[c] Netherlands Organisation for Applied Scientific Research (TNO), Delft, the Netherlands
[d] National Laboratory for Civil Engineering (LNEC), Lisbon, Portugal

HIGHLIGHTS

- A cyclic joint constitutive model is proposed for the Distinct Element Method framework.
- The model integrates a yield surface, softening laws, and energy dissipation.
- A novel exponential dilatancy-decay law is embedded in a standard uplift-correction contact update.
- The model is validated against material and full-scale structural tests.
- Simulations accurately capture rocking, shear, and hybrid failure modes.

ARTICLE INFO

Keywords:
Unreinforced masonry
Distinct element method
Constitutive model
Multi-surface plasticity
Damage mechanics
Cyclic behavior

ABSTRACT

This paper presents a cyclic joint constitutive model within a Distinct Element Method framework to simulate the in-plane response of unreinforced masonry structures. The model combines multi-surface failure criteria, including tensile cut-off, Coulomb friction, and an elliptical compression cap. It incorporates exponential softening, a unified damage scalar for stiffness degradation, and a hardening–softening law for compression. Shear-induced dilatancy is captured via an uplift-correction mechanism with an exponential dilatancy-decay law, while stiffness degradation governs energy dissipation. The model is validated at both material and structural scales. Material-level simulations of cyclic compression and shear tests show close agreement with experimental data. Structural-scale validation on full-height calcium-silicate walls under combined compression and cyclic lateral loading demonstrates the ability to reproduce rocking-dominated, shear-dominated, and hybrid failure mechanisms . The model successfully replicated global hysteretic force–drift loops, capturing stiffness decay and energy dissipation, as well as local failures like cracking, sliding, and toe crushing. The model also reproduced the drift-dependent transition from rocking to friction-controlled sliding, a key mechanism for earthquake assessment. By integrating these features into a single, efficient framework, the proposed constitutive model provides a robust tool for evaluating seismic performance and conserving heritage.

1. Introduction

Until now, masonry has remained one of the most widespread and historically important construction materials worldwide. However, its inherently heterogeneous and quasi-brittle nature poses ongoing challenges for accurate numerical modelling, both at the material and structural scales. Over the past few decades, significant progress in computational mechanics has led to the development of increasingly sophisticated constitutive models for simulating the mechanical behavior of masonry structures under various loading scenarios. According to the classification by Lourenço [1], modelling strategies can be broadly divided into three categories. Macro-modelling approaches either represent masonry as an equivalent frame [2–4] or treat it as a homogenized continuum [5–7]. Simplified micro-modelling strategies represent the

* Corresponding author.
Email address: y.p.oktiovan@tudelft.nl (Y.P. Oktiovan).

https://doi.org/10.1016/j.compstruc.2025.108094
Received 22 September 2025; Accepted 29 December 2025
Available online 2 January 2026

brick units as rigid or deformable blocks, while the mortar joints are captured using zero-thickness interfaces [8–12]. Finally, detailed micro-modelling strategies discretise both the units and mortar joints explicitly as separate deformable components [13–15]. Each of these strategies offers a trade-off between computational cost and modelling fidelity, influencing their applicability depending on the scale and objectives of the analysis. Among them, the simplified micro-modelling approach offers a particularly effective compromise, striking a balance between computational efficiency and numerical accuracy. By concentrating the nonlinear response within the interface elements, the overall model remains tractable while still capturing key mechanical behaviors. However, this also means that the fidelity of the simulation strongly depends on the accurate characterization of cohesive-frictional interface behavior.

To this end, numerous researchers have developed damage-plasticity interface models to simulate the nonlinear behavior of masonry structures [10,11,16–19]. These models are capable of capturing the degradation of tensile and shear strength through damage mechanics, along with irreversible deformations and frictional sliding that occur after yielding. In the early development of the interface model for masonry structures, Lotfi and Shing [17] proposed a single hyperbolic surface for tension and shear without a compression cap. Lourenço and Rots [19] introduced a compression cap and separate yield criteria for shear and tension, although this led to numerical issues at yield surface intersections (“corner” regions). Macorini and Izzuddin [11] addressed this by proposing a unified model with a compression cap and a single hyperbolic yield surface, enhancing stability and smoothness. Nie et al. [16] explored this unified yield surface under the effective stress spaces with a non-shrinking compression cap upon crushing.

The models described above have typically been implemented within finite element frameworks using incremental-iterative solution procedures. While effective in many cases, these methods often encounter convergence difficulties under highly nonlinear conditions, particularly during cyclic loading and simulations that approach structural collapse. To mitigate this, methods such as closest point projection [20,21] and radial return [22] have been proposed, often combined with a line search method [23] or a substepping scheme [24]. Other solutions that do not involve implicit-based solvers have also been explored, such as the use of the Forward Euler method [25], or event-based sequentially linear analysis [26,27].

With the continuing growth in computational resources, the distinct element method (DEM) has emerged as a powerful alternative for modelling masonry structures. DEM employs a conditionally stable explicit time integration scheme, which facilitates simulations up to collapse without the convergence issues typically encountered in traditional implicit solvers. This makes DEM particularly attractive for the analysis of large-scale or historic masonry structures, where complex failure modes must be captured [28–31]. However, the predictive accuracy of DEM hinges on robust contact constitutive models that offer appropriate nonlinear behavior of the analyzed discontinuous medium. Without such formulations, key phenomena, such as hysteretic loops, residual drift, and transitions between different failure modes, cannot be reliably captured in DEM.

Several DEM contact models have been proposed to better represent the mechanical behavior of masonry constituents. Pulatsu [8] and Oktiovan et al. [12] formulated damage–plasticity contacts with a compression cap to capture shear–compression coupling. The former adopted linear softening in tension, shear, and compression, whereas the latter employed piecewise-linear softening in tension and shear, along with a hardening–softening law in compression. Both of these cap-based formulations, however, were calibrated and validated only under monotonic loading, limiting their demonstrated capability under cyclic demand (e.g., load reversals, degradation, and pinching).

In parallel, DEM strategies for URM structures under quasi-static and cyclic loading have emphasized block–interface formulations. Malomo et al. [32] used elasto-plastic deformable blocks (i.e., blocks with limited tensile and compressive strengths) with Mohr–Coulomb interfaces and a tension cut-off, while Damiani et al. [33] advanced this approach by combining elasto-plastic blocks with a refined interface model [8]. More recently, Pulatsu et al. [34] examined cyclic in-plane response within a DEM framework but represented shear–compression coupling with a compression cut-off (i.e., without a compression cap).

This study presents a contact constitutive model within the DEM framework tailored for the cyclic loading of masonry assemblies. The formulation is also applicable to other block-based systems in which local cohesive or frictional interactions govern the macroscopic response of the discontinuum. The main contribution is a unified definition of the masonry joint behavior under cyclic demand. The joint constitutive law integrates multi-surface plasticity with exponential softening in tension and shear, a hardening-softening evolution in compression, a dilatancy-induced uplift mechanism, and a nonlinear, energy-dissipative unloading/reloading algorithm. The modelling strategy is implemented in *3DEC*, a commercial software for DEM, which uses an explicit time-marching integration scheme, avoiding substepping and iterative return mapping while maintaining numerical stability under large displacements. The model is validated against cyclic uniaxial compression, direct-shear, and shear–compression triplet tests, as well as full-scale in-plane wall experiments. This demonstrates the model’s capability to match both global force–drift loops and detailed crack patterns, and to reproduce the intricate transition from rocking to sliding mechanisms, including hinge formation, progressive sliding, and toe crushing, offering a robust tool for seismic assessment of masonry structures.

The present work focuses only on in-plane loading; the out-of-plane (OOP) behavior is not addressed. This scope was chosen to isolate the shear–compression–tension mechanisms at bed and head joints that dominate in-plane seismic response and for which standardized cyclic datasets enable rigorous calibration. While the formulation is general and compatible with 3D analyses, extending and calibrating the model for OOP loading cases and coupled in-plane–OOP demands is left for future work.

2. Formulation of the cyclic joint constitutive model

The proposed formulation is developed within the distinct element method (DEM) framework [35], which falls under the simplified micro-modelling approach as categorized by Lourenço [1].

This approach represents masonry units as rigid or deformable blocks with extended dimensions to cover mortar joints, thereby replicating masonry structures as a group of discrete blocks. The deformable blocks may be considered as an elastic or elasto-plastic continuum. The mortar joints are represented as a set of cohesive-frictional contact points, as shown in Fig. 1. In this study, the masonry units are treated as rigid bodies with a potential crack plane at the unit’s mid-length (dashed red line in Fig. 1). Consequently, their elastic deformability is accounted for, and the block’s Young’s modulus is not used in the stiffness update. The overall elastic compliance of the assemblage is lumped at the interfaces via normal and shear springs (k_n and k_s, respectively), which govern the initial stiffness and are first estimated via homogenization and then calibrated to tests.

As the blocks in contact are detected through the ’common-plane’ concept [35], the contact points between adjacent blocks are automatically generated when the gaps measured from the direction normal to this fictitious plane are less than the given tolerance. The number of the generated contact points depends on the adopted face triangulation algorithm (readily available in the software). Fig. 1, shows a mesh termed as “radial-8” where each face of the block has a center vertex and an extra vertex at the mid-edge, creating 9 contact points at each face of the block.

Under DEM, the proposed formulation is solved using the explicit time-marching integration scheme, where the equation of motion, presented in Eq. (1) for a single block i, is solved at each timestep to obtain the new block positions and displacement increment.

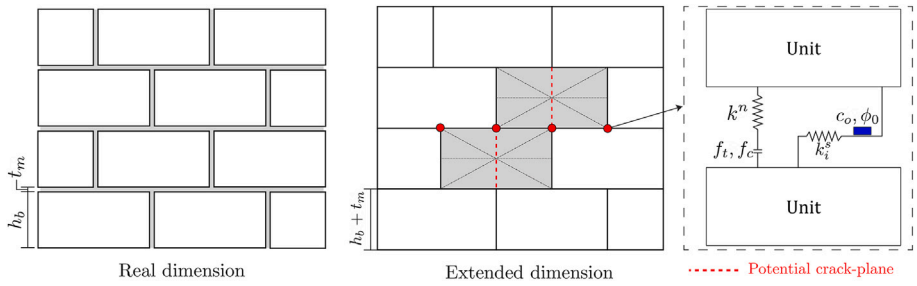

Fig. 1. Discretization of the masonry constituents according to the distinct element method (DEM).

$$m_i\, d\mathbf{v}_i = \left[\left(\sum_{j\in C_i} \mathbf{F}_{i,j}^{\mathrm{c},t}\right) + \mathbf{F}_i^{\mathrm{ext},t} + \mathbf{F}_i^{\mathrm{w},t} - \mathbf{F}_i^{\mathrm{d},t}\right] dt \tag{1}$$

where m is the block mass, $\mathbf{v}$ is the velocity vector, C_i is the set of contact points governing block i, $\mathbf{F}_{i,j}^{\mathrm{c},t}$ is the contact force vector at point j along the block's boundary, $\mathbf{F}_i^{\mathrm{ext},t}$ is the external force vector, $\mathbf{F}_i^{\mathrm{w},t}$ is the body force vector, and $\mathbf{F}_i^{\mathrm{d},t}$ is the damping force vector. Similarly, the rotational motion is defined in Eq. (2)

$$\mathbf{I}_i d\boldsymbol{\omega}_i = \left(\mathbf{M}_i^t - \mathbf{M}_i^{\mathrm{d},t}\right) dt \tag{2}$$

where $\mathbf{I}$ is the moment of inertia, $\boldsymbol{\omega}$ is the rotational velocity vector, $\mathbf{M}^t$ is the moment applied to the block, and $\mathbf{M}^{\mathrm{d},t}$ is the damping moment.

These equations are discretized using a staggered scheme. Let t denote a generic time level and Δt denote the constant time step. We introduce the half-step times $\left[t^- = t - \Delta t/2, t^+ = t + \Delta t/2\right]$. Translational and rotational velocities are stored and updated at half-time steps, while forces and moments are evaluated at integer time levels t. Integrating the equations of motion over the interval $\left[t^-, t^+\right]$ yields:

$$m_i \int_{t^-}^{t^+} d\mathbf{v}_i = \int_{t^-}^{t^+} \left[\left(\sum_{j\in C_i} \mathbf{F}_{i,j}^{\mathrm{c},t}\right) + \mathbf{F}_i^{\mathrm{ext},t} + \mathbf{F}_i^{\mathrm{w},t} - \mathbf{F}_i^{\mathrm{d},t}\right] dt \tag{3}$$

The left-hand side of Eq. (3) can be evaluated exactly and defines the finite velocity increment:

$$\Delta\mathbf{v}_\mathbf{i}^t := \mathbf{v}_i^{t^+} - \mathbf{v}_i^{t^-} \tag{4}$$

Using a midpoint approximation of the time integral, the forces are evaluated at t, and the discrete translational update becomes:

$$m_i \Delta\mathbf{v}_i^t \approx \left[\left(\sum_{j\in C_i} \mathbf{F}_{i,j}^{\mathrm{c},t}\right) + \mathbf{F}_i^{\mathrm{ext},t} + \mathbf{F}_i^{\mathrm{w},t} - \mathbf{F}_i^{\mathrm{d},t}\right] \Delta t \tag{5}$$

An analogous procedure is applied to the rotational equation. Integration over the interval $\left[t^-, t^+\right]$ yields:

$$\mathbf{I}_\mathbf{i} \int_{t^-}^{t^+} d\boldsymbol{\omega}_i = \int_{t^-}^{t^+} \left(\mathbf{M}_i^t - \mathbf{M}_i^{\mathrm{d},t}\right) \mathrm{d}t, \tag{6}$$

which gives the angular velocity increment:

$$\Delta\boldsymbol{\omega}_\mathbf{i}^t := \boldsymbol{\omega}_i^{t+} - \boldsymbol{\omega}_i^{t-}, \tag{7}$$

which leads, after the midpoint approximation of the contribution, to:

$$\mathbf{I}_\mathbf{i}\, \Delta\boldsymbol{\omega}_\mathbf{i}^t \approx \left(\mathbf{M}_i^t - \mathbf{M}_i^{\mathrm{d},t}\right) \Delta t. \tag{8}$$

For completeness, it is important to note that orientations are advanced with a small-rotation update, and that the scheme is employed in a quasi-static, dynamic-relaxation sense with small local damping and energy/residual checks. These additions make the time-integration procedure self-contained without altering any results.

The damping force $\mathbf{F}_\mathbf{i}^{\mathrm{d},t}$ and moment $\mathbf{M}_\mathbf{i}^{\mathrm{d},t}$ are included in Eqs. (1) and (2), respectively, as local numerical damping [36] used in a dynamic-relaxation sense to obtain quasi-static equilibria with the explicit scheme. Contact opening/closure and softening often introduce high-frequency oscillations that would require impractically small timesteps to settle without this local damping. These terms attenuate spurious kinetic energy and align the unbalanced force/moment with the current velocity directions. They are not physical dissipation models and do not alter the conditional stability. These are defined based on the proportion of the unbalanced or net force/moment and the direction of the velocity (or rotational velocity) vectors at t^-. These are expressed as follows:

$$\mathbf{F}_i^{d,t} = \alpha \left\| \sum \mathbf{F}_i^t \right\| \mathrm{sgn}\left(\mathbf{v}_i{}^{t^-}\right) \quad \text{and} \quad \mathbf{M}_\mathbf{i}^{\mathrm{d},t} = \alpha \left\| \sum \mathbf{M}_i^t \right\| \mathrm{sgn}\left(\boldsymbol{\omega}_i^{t^-}\right) \tag{9}$$

where $\sum \mathbf{F}_i^t$ and $\sum \mathbf{M}_i^t$ are the unbalanced force and moment, respectively, and $\mathrm{sgn}\left(\mathbf{v}^{t^-}\right)$ and $\mathrm{sgn}\left(\boldsymbol{\omega}^{t^-}\right)$ denote the signum function that defines the opposite direction of the translational $\mathbf{v}^{t^-}$ and rotational $\boldsymbol{\omega}^{t^-}$ velocities at t^-, respectively. Throughout the simulations in this paper, the local damping constant α is set to 0.8 by default.

Although the equations of motion in Eqs. (1) and (2) are integrated explicitly with the inertial term, the analysis is carried out in a quasi-static (dynamic-relaxation) fashion. Inertia and local damping serve only to relax each load increment into equilibrium. For each step, the pseudo-time is advanced under slow loading due to the significantly small Δt while keeping the residual force norm $\|\mathbf{R}_i\|$ small, i.e.:

$$\frac{\|\mathbf{R}_i\|}{\|\mathbf{F}_i^{ext}\|} \quad \text{where} \quad \mathbf{R}_i = \sum \mathbf{F}_i^c + \mathbf{F}_i^{ext} + \mathbf{F}_i^w - \mathbf{F}_i^d \approx 0 \tag{10}$$

The converged configuration under these criteria is then taken as the static response. Once the updated velocities are obtained, i.e. $\mathbf{v}^{t^+}$ and $\boldsymbol{\omega}^{t^+}$, the positions of the blocks centroid are updated as:

$$\mathbf{x}_i(t + \Delta t) = \mathbf{x}_i(t) + \mathbf{v}_i^{t^+} \Delta t \tag{11}$$

where $\mathbf{x}$ is the block centroid's positional vector. The new locations of block vertices are updated accordingly, considering the incremental rotation calculated from the angular velocities multiplied by Δt.

Each contact point comprises three orthogonal springs, one in the normal direction and the other two in the shear directions. Under the linear elastic range, the normal and shear force increments at the contact points are defined according to the respective displacement increments, as presented in Eq. (12).

$$\Delta F^n = k^n A^c \Delta u^n \quad \text{and} \quad \Delta\mathbf{F}^\mathbf{s} = k^s A^c \Delta\mathbf{u}^\mathbf{s} \tag{12}$$

where F^n, k^n, and u^n are the normal force, normal stiffness, and normal displacement, respectively, while $\mathbf{F}^\mathbf{s}$, k^s, and $\mathbf{u}^\mathbf{s}$ are the shear force vector, shear stiffness, and shear displacement vector, respectively, and A^c is the tributary area [12].

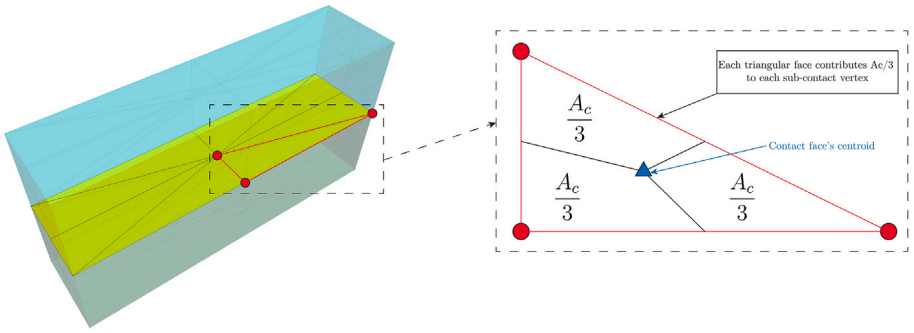

Fig. 2. Construction of the sub-contact area A_c for force mapping.

Here, A_c denotes the sub-contact area used to map interface reactions to nodal forces. As illustrated in Fig. 2, the contact region on the interface plane is first decomposed into triangular planes. For one sub-contact point, the associated area is constructed by assigning one-third of each triangular face that contains the sub-contact and lies on the contact plane. This equal partition ensures a consistent and objective distribution of the contact area among neighbouring sub-contacts.

The resulting region is then intersected with the opposing block's face lying on the same plane, yielding the effective sub-contact area A_c used in the force and energy mapping. For face-to-face contacts, the construction is applied independently to each block. Since sub-contacts are defined at the nodes of both blocks, two parallel interface contributions arise, and the effective area associated with each sub-contact is therefore halved.

It is important to emphasize that the explicit time marching integration scheme employed in the discrete element method (DEM) is only conditionally stable, with stability governed by the critical time step defined in Eq. (13) [37]:

$$\Delta t_{block} = \frac{2}{\omega_{max}} \tag{13}$$

where t_{block} is the maximum stable timestep and ω_{max} is the highest system frequency . Eq. (13) provides a conservative estimate for the stable time increment by considering the upper bound associated with the highest eigenfrequency of the system. This criterion has been shown to offer sufficient stability for complex, nonlinear systems [38,39]. The stable timestep in Eq. (13) is essentially independent of the local numerical damping used for dynamic relaxation in Eq. (1). The damping parameter α serves only to attenuate spurious oscillations and does not alter the conditional-stability nature of the method.

In this paper, the constitutive model that defines the nonlinear behavior of masonry structures under monotonic loading, previously proposed by the authors [12], is extended to include the dilatancy softening of the mortar layer when subjected to shear and compression loading as well as the extension to include stiffness degradation in tension, shear, and compression regimes.

2.1. Overview of the monotonic joint constitutive model

The mechanical response of the joint model representing the unit-mortar interface under monotonic loading conditions is characterized by the traction-separation laws in tension, shear, and compression, coupled with a multi-surface plasticity model. Fig. 3 shows the adopted joint constitutive model, which encompasses the softening behavior in tension (Fig. 3(A)), shear (Fig. 3(B)), and a nonlinear compressive behavior (Fig. 3(C)). The multi-surface plasticity model in Fig. 3(D)) comprises a tensile cut-off F_1 (Eq. 14), a Coulomb friction yield line F_2 (Eq. 15), and a compression cap F_3 (Eq. 16) to limit the behavior of the interface under shear–compression.

$$F_1 = \sigma^n - f_t(u_t^n) \tag{14}$$

$$F_2 = \left\|\boldsymbol{\tau}\right\| + \sigma_n \tan\left(\phi_{cv} + \psi(\mathbf{u}^s)\right) - c(\mathbf{u}^s) \tag{15}$$

$$F_3 = C_{nn}\,\sigma_n^2 + C_{ss}\left\|\boldsymbol{\tau}\right\|^2 + C_n\,\sigma_n - [\sigma^n(u_c^n)]^2 \tag{16}$$

where u_c^n and u_t^n are the relative normal subcontact displacements in compression and tension, respectively, σ^n is the normal stress, $\boldsymbol{\tau}$ is the shear stress vector, ϕ_{cv} is the friction angle at constant volume, $f_t(u_t^n)$ is the tensile strength that reduces according to the tensile normal displacement u_t^n, $c(\mathbf{u}^s)$ is the cohesive strength that decays depending on the shear displacement vector $\mathbf{u}^s$, $\psi(\mathbf{u}^s)$ is the dilatancy angle corresponding to the shear displacement vector, $\sigma^n(u_c^n)$ is the compressive strength that evolves under the compressive normal displacement u_c^n, C_{nn} and C_{ss} are the parameters that control the radius of the elliptical curve in Fig. 3(D), and C_n is the ellipsis center.

In contrast to the previous study by the authors [40], where a piecewise linear softening law is used on the tensile and shear regimes to provide flexibility for the users to fit the strength degradation given the material characterization tests, an exponential softening law is used in this joint constitutive model to reduce the number of parameters needed by the users, and to achieve a smoother strength degradation on each regime. The exponential softening laws for tension and shear are given in Eqs. (17) and (18), respectively.

$$f_t(u_t^n) = \left[1 - d_t(u_t^n)\right]\ f_t, \qquad d_t(u_t^n) = 1 - exp\left[-\frac{f_t}{G_f^I}\left(u_t^n - \frac{f_t}{k^n}\right)\right] \tag{17}$$

$$\boldsymbol{\tau}(\mathbf{u}^s) = c(\mathbf{u}^s) - \sigma^n \tan\left(\phi_{cv} + \psi_0\right) \tag{18}$$

where $d_t(u_t^n)$ is the tensile damage scalar, f_t is the tensile strength, G_f^I is the mode-I fracture energy, and $\boldsymbol{\tau}(\mathbf{u}^s)$ is the post-peak shear stress. The exponential softening law for shear strength is implemented to the cohesive strength, defined in Eq. (19).

$$c\left(\mathbf{u}^s\right) = \left[1 - d_s\left(\mathbf{u}^s\right)\right] c_0, \qquad d_s\left(\mathbf{u}^s\right) = 1 - \exp\left[-\frac{c_0}{G_f^{II}}\left\langle \left\|\mathbf{u}^s\right\| - u_{el}^s \right\rangle_+\right] \tag{19}$$

where $d_s(\mathbf{u}^s)$ is the shear damage scalar, G_f^{II} is the mode-II fracture energy, and u_{el}^s is the elastic shear displacement, defined by Eq. (20).

$$u_{el}^s = \frac{\tau_{max}}{k_s} = \frac{c_0 - \sigma^n \tan\left(\phi_{cv} + \psi_0\right)}{k^s} \tag{20}$$

where c_0 is the peak cohesive strength, and ψ_0 is the initial dilatancy angle. It is important to note that the default implementation assumes a fixed value of dilatancy. The dilatancy softening effect is discussed

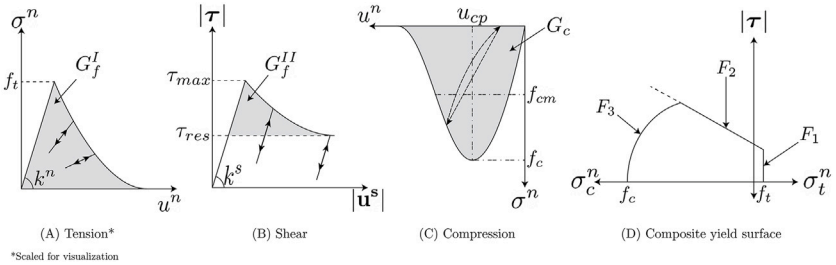

Fig. 3. Illustration of the proposed joint constitutive model.

in the following sub-section. To couple the post-peak softening isotropically [1,8,16], a combined damage scalar d_{ts} that couples both the tensile and shear behaviors is introduced in Eq. (21), replacing the tensile d_t and shear d_s damage scalars in Eqs. (17) and (19), respectively. To prevent round-off accumulation error, both $f_t(u_t^n)$ and $c(\mathbf{u}^s)$ are capped at 1×10^{-12} according to the precision limit of the user-defined model in 3DEC [41], the commercial software for DEM.

$$d_{ts}(u^n,) = d_t(u^n) + d_s(\mathbf{u}^s) - d_t(u^n)d_s(\mathbf{u}^s) \tag{21}$$

The uniaxial compressive behavior of the joint constitutive model is governed by the hardening/softening law introduced by Lourenço and Rots [19]. After the linear elastic phase reaches 20 % of the compressive strength, the interface enters the hardening phase defined by the parabolic function in Eq. (22).

$$\sigma^n(u_c^n) = \sigma_{el}^n + (f_c - \sigma_{el}^n)\sqrt{\frac{2(u_c^n - u_{el}^n)}{u_{cp}} - \frac{(u_c^n - u_{el}^n)^2}{u_{cp}}} \tag{22}$$

where $\sigma^n(u_c^n)$ is the normal compressive stress, σ_{el}^n is the elastic compressive stress set at 20 % of the compressive strength f_c, u_{el}^n is the normal displacement at elastic compressive stress, i.e., $0.2f_c/k^n$, and u_{cp} is the displacement at compressive strength, set as a user supplied multiplier n times f_c/k^n, the supposed displacement at compressive strength according to the initial normal stiffness k^n.

The user-supplied n factor creates flexibility for the user to set the hardening behavior, as some masonry exhibits a relatively ductile behavior up to two or three times the supposed elastic displacement at peak compressive strength. [42] The softening phase is defined through a compressive damage scalar $d_c(u_c^n)$ in Eq. (23). This damage scalar is correlated to the normal compressive displacement u_c^n, as defined in Eq. (24).

$$\sigma^n(u_c^n) = \left[1 - d_c(u_c^n)\right] f_c \tag{23}$$

$$d_c = \begin{cases} 0, & u_c^n < u_{cp} \\ \left(1 - \frac{f_{cm}}{f_c}\right)\left(\frac{u_c^n - u_{cp}}{u_{cm} - u_{cp}}\right)^2 & u_{cp} \le u_c^n < u_{cm} \\ \left(1 - \frac{f_{cr}}{f_c}\right) - \frac{f_{cm} - f_{cr}}{f_c}\exp\left(2\frac{f_{cm} - f_{cp}}{u_{cm} - u_{cp}}\frac{u_c^n - u_{cm}}{f_{cm} - f_{cr}}\right) & u_c^n \ge u_{cm} \end{cases} \tag{24}$$

where f_{cm} is the intermediate post-peak compressive stress, the inflection point from quadratic softening to exponential, u_{cm} is the corresponding displacement at f_{cm}, and f_{cr} is the residual compressive strength.

The compressive damage scalar is correlated to the compressive fracture energy, G_c, by setting the intermediate displacement u_{cm} such that the area under the curve in Fig. 3(C) corresponds to that of the multilinear softening law. The correlation is performed mathematically using Eq. (25) [12].

$$u_{cm} = \frac{G_c - 0.5\frac{f_c^2}{9k^n} - 0.65(u_{cp} - u_{el}^n)f_c + 0.75u_{cp}f_c + 0.25u_{cp}f_{cr}}{u_{cp}f_c + u_{cp}f_{cr}}u_{cp} \tag{25}$$

where G_c is the compressive fracture energy, and u_{el}^n is the displacement at elastic compressive stress σ_{el}^n, i.e. $\sigma_{el}^n \,/\, k^n$.

2.2. Inclusion of the dilatancy softening

Based on the experimental tests on masonry couplets conducted by several researchers [13,43–46], it has been observed that the normal displacement of the joints induced by dilation gradually decreased with continued shear loading, eventually reaching a small constant value or zero in some cases. Multiple researchers have proposed numerical modelling strategies to address the dilatancy effect observed in mortar joints through the interface constitutive model. Lourenço and Rots [19] and Giambanco et al. [47] started including the dilatancy effect through the non-associative flow rule, with a dilatancy angle that was separated from the friction angle. This dilatancy angle also decreased with increasing normal pressure for Lourenço and Rots [19], while Giambanco et al. [47] associated the decrease with the loss of cohesive strength. Van Zijl [46] extended the approach from Lourenço and Rots [19], to consider the volumetric increase that caused the uplift of masonry units when subjected to shear load. Andreotti et al. [13] proposed a data-driven strategy to calibrate the dilatancy angle based on the experimental data. The dilatancy angle was coupled to the friction angle, and the decrease was related to the plastic shear and normal displacements from the experiments.

As shown in Eq. (15), the Coulomb friction line F_2 departs from the formulation of Oktiovan et al. [12] by adopting the shear-strength definition of Andreotti et al. [13], in which the friction coefficient is expressed as the sum of a constant-volume friction angle, ϕ_{cv}, and a dilatancy angle, ψ, that decays with accumulated plastic slip.

It has been described by several authors [1,13,43,44] that ϕ_{cv} reflects the surface roughness governing sliding resistance, while ψ controls the joint opening or inclination of the sliding surface as shear slip develops. Furthermore, as the shear displacement increases, the uplift/dilatant displacement reaches a relatively constant value, which is interpreted as the smoothened bed-joint due to the fully decayed dilatancy angle (Fig. 4(D)) [46].

The above behavior is illustrated in Fig. 4. At the initial state (Fig. 4(A)), the shear stress is defined as given in Eq. (18), where the friction angle at constant volume ϕ_{cv} is added to the initial dilatancy angle ψ. As the crack through the joint develops (Fig. 4(B)), the cohesion and the dilatancy angle soften. This differs from the previous formulation defined by the authors [12] and the typical interface-based constitutive model for masonry that considers dilatant behavior [9,16,19,25,46]. While the cohesive strength softens according to the combined damage scalar d_{ts} (Eq. 19), the dilatancy angle decays according to the ratio of normal confining stress and the stress at zero dilation, expressed in Eq. (26) [48].

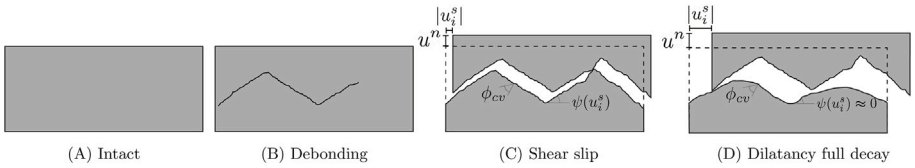

Fig. 4. Phases of the mortar joints when subjected to shear load [13].

$$\psi(\mathbf{u}^{\mathbf{s}}) = \begin{cases} \psi_0 \left(1 - \dfrac{\|\mathbf{u}^{\mathbf{s,p}}\|}{u^{s,\max}}\right) \exp\left[-\delta\left(\|\mathbf{u}^{\mathbf{s,p}}\|\right)\right] & \|\mathbf{u}^{\mathbf{s,p}}\| \le u^{s,\max} \\ 0 & \|\mathbf{u}^{\mathbf{s,p}}\| > u^{s,\max} \end{cases} \tag{26}$$

where δ is the softening gradient [46], $\mathbf{u}^{\mathbf{s,p}}$ is the plastic shear displacement vector and $u^{s,\max}$ is the shear displacement at zero dilation. If the plastic displacement exceeds the limiting displacement at zero dilation, the decay is capped at zero to ensure thermodynamic consistency.

As the shear damage accumulates (Fig. 4(C)), plastic slip initiates as soon as the shear traction reaches the Coulomb friction line in Fig. 3(D). After the onset, the slip evolves while the cohesive strength softens and the dilatant part of Eq. (15) decays according to Eq. (26). When cohesion has fully degraded ($c \to 0$) and $\psi \approx 0$, the residual shear strength is purely frictional. The mathematical definition in Eq. (18) shows that at large slips, the tangential response tends to the frictional branch. The physical representation of the dilatancy softening is shown in Fig. 4(D), which shows that the surface of asperities softens as shear slip progresses [13,48].

To represent the uplift in the normal direction, the normal displacement increment (Δu^n in Eq. (12)) is adjusted according to the magnitude of the shear displacement increment $|\Delta \mathbf{u}^{\mathbf{s}}|$ and the dilation coefficient. This is mathematically expressed in Eq. (27).

$$\Delta u^n := \begin{cases} \Delta u^n + \|\Delta \mathbf{u}^{\mathbf{s}}\| \tan(\psi(\mathbf{u}^{\mathbf{s}})) & \|\mathbf{u}^{\mathbf{s}}\| <= \|u^{s,\max}\| \\ \Delta u^n & \|\mathbf{u}^{\mathbf{s}}\| > u^{s,\max} \end{cases} \tag{27}$$

As an explicit integration scheme is used as the solution procedure, the normal force increment calculated in Eq. (12) is corrected to account for the dilatancy effect, shown in Eq. (28).

$$F^n := F^n + k^n A^c |\Delta \mathbf{u}^{\mathbf{s}}| \tan(\psi(\mathbf{u}^{\mathbf{s}})) \tag{28}$$

Upon unloading in shear, the yield condition is inactive, so only elastic closure can occur. The accumulated plastic offset and current dilation angle are retained (i.e., no healing), matching the partial recovery observed in experimental tests.

It is important to note that, even though the shear stress in Eq. (18) considers the contribution of friction and dilation even in the linear elastic state, the correction due to uplift in the normal direction (Eq. 27) only considers the dilatancy effect. As shown in Fig. 4(C) and Fig. 4(D), the roughness of the surface of asperities that mobilize the uplift movement is caused only by the dilatant behavior of the mortar layer. Furthermore, it is essential to highlight that this uplift-correction framework is well-established as proposed by Van Zijl [46] and Andreotti et al. [13] . The contribution of this paper lies in the exponential dilatancy decay law and its consistent integration into the DEM framework.

2.3. Extension to include energy dissipation mechanisms

The main improvement over the previous joint constitutive model [12] is the energy dissipation framework, which captures damage accumulation under cyclic loading. Dissipation is activated in a fracture mode-dependent way through controlled stiffness degradation. In tension, unloading follows a secant rule (see Fig. 3(A)): the unloading stiffness is the secant from the origin to the current point on the degraded tensile envelope, so the apparent joint stiffness decreases as the normal opening grows. The stiffness degradation rate corresponds to the combined tensile-shear damage scalar Eq. (21), as presented in Eq. (29).

$$k^n(d_{ts}) = (1 - d_{ts})k^n \tag{29}$$

Elastic unloading is used in the shear regime (Fig. 3), where the initial shear stiffness k_i^s is maintained as the shear displacement progresses. This is consistent with the hypotheses adopted by other authors [6,25,49] as well as the experimental results obtained from the cyclic direct shear test [50].

The unloading mechanism used in the compression regime follows the nonlinear unloading/reloading formulation defined by Facconi et al. [51], as illustrated in Fig. 5. Experimental results on uniaxial compression tests of masonry wallets [51–55] showed that the masonry composite unloads in a nonlinear manner with irreversible strain (or deformation) and stiffness degradation to account for energy dissipation.

Leveraging the robustness of the explicit time marching integration scheme, a nonlinear unloading branch is proposed, as shown in Fig. 5(A). The unloading branch reaches a normal plastic displacement $u_{n_{pl}}$ at zero compressive stress, which defines the irrecoverable damage of the masonry assemblage due to loading and unloading sequences. The normalized plastic compressive displacement in Eq. (30), adapted from [51], separates the plastic component after the onset of compressive failure and is derived under a small-displacement assumption to ensure compatibility when expressed in terms of displacement.

$$u'_{n_{pl}} = \begin{cases} 0.47\,(u'_{n_{un}})^2 + 0.5\,|u'_{n_{un}}|, & dc = 0, \\ 1.175\,(u'_{n_{un}})^2 + 1.25\,|u'_{n_{un}}|, & dc > 0\,. \end{cases} \tag{30}$$

where $u'_{n_{pl}}$ is the normalized plastic compressive displacement, and $u'_{n_{un}}$ is the normalized unloading displacement. Both values are normalized against the peak compressive displacement u_{cp} (Fig. 3(C)). The unloading branch is defined nonlinearly and is correlated to the unloading displacement $u_{n_{un}}$ and the plastic strain $u_{n_{pl}}$. The general formulation is defined in Eq. (31).

$$\sigma_c^n = f_{c_{re}} + \left(f_{c_{un}} - f_{c_{re}}\right) \frac{B_1 \chi + \chi^2}{1 + B_2 \chi + B_3 \chi^2} \tag{31}$$

where

$$\chi = \frac{u_c^n - u_{n_{un}}}{u_{n_{pl}} - u_{n_{un}}} \tag{32}$$

where σ_c^n is the current normal compressive stress during unloading, $f_{c_{re}}$ and $f_{c_{un}}$ are the reloading and unloading compressive stresses, respectively, and B_1, B_2, and B_3 are the variables determining the shape of the unloading branch (Eq. 33).

$$B_1 = \frac{k_{n_{un}}}{E_s}; \quad B_2 = B_1 - B_3; \quad B_3 = 2 - \frac{k_{n_{pl}}}{E_s}(1 + B_1); \tag{33}$$

where $E_s = f_{c_{un}}/(u_{n_{un}} - u_{n_{pl}})$, the secant stiffness between the onset of unloading and the plastic displacement (from Eq. (30)), $k_{n_{un}}$ and $k_{n_{pl}}$ are

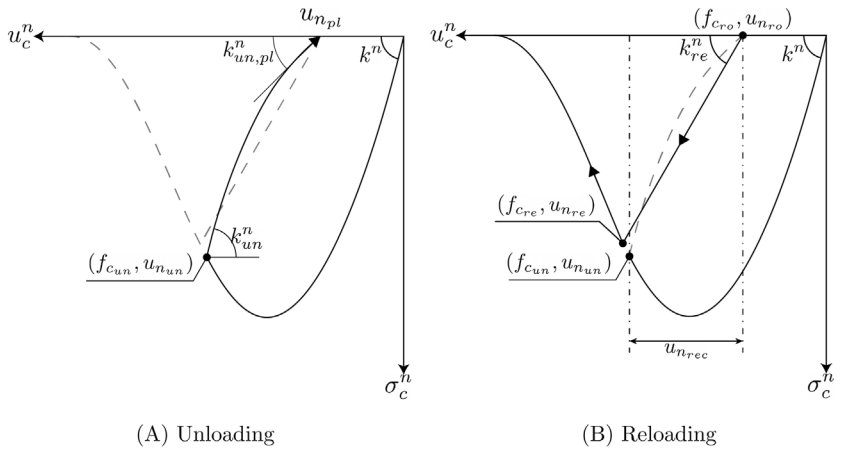

Fig. 5. Nonlinear unloading mechanism for the compressive behavior of masonry assemblage [51].

the unloading and plastic tangent stiffnesses (Fig. 5(A)), respectively. Both values are defined according to Eq. (34).

$$k_{n_{un}} = \gamma_{un} k_n; \quad k_{n_{pl}} = \frac{\gamma_{pl} k_n}{\left(1 + \frac{u_{n_{un}}}{u_{cp}}\right)^e} \tag{34}$$

where $\gamma_{un} = 1.5$, $\gamma_{pl} = 0.15$, and $e = 2$, empirically defined according to the suggestions provided by Facconi et al. [51], where e defines the nonlinear curve close to the plastic displacement and the point of inflection between $k_{n_{un}}$ and $k_{n_{pl}}$. Those variables were determined from the best fitting of the unloading curves of a uniaxial compression test on masonry wallets gathered from the literature.

The reloading branch (Fig. 5(B)) starts when compressive displacement increases after either complete (when the compressive stress reaches zero) or partial unloading [51]. Due to damage accumulated during the cyclic loading sequence, the reloading curve typically intersects the envelope curve at a displacement larger than the displacement level during the unloading onset [56]. With that in mind, the linear reloading mechanism is adopted in this model, deviating from the nonlinear representation defined by Facconi et al. [51], to simplify the formulation. Furthermore, several authors [56–58] have shown that the linear representation of the reloading sequence is adequate to simulate a masonry assemblage's energy dissipation mechanism under uniaxial cyclic compression. The linear reloading compressive stress is defined in Eq. (35).

$$\sigma_c^n = f_{c_{ro}} + k_{re}^n (u_c^n - u_{n_{ro}}) \tag{35}$$

where $f_{c_{ro}}$ and $u_{n_{ro}}$ are the compressive stress and displacement at the onset of reloading, and k_{re}^n is the reloading stiffness, defined in Eq. (36).

$$k_{re}^n = \frac{\beta_d f_{c_{un}} - f_{c_{ro}}}{u_{n_{un}} - u_{n_{ro}}} \tag{36}$$

where

$$\beta_d = \begin{cases} \dfrac{1}{1 + 0.2(u'_{n_{rec}})^{0.5}} & \text{for} \quad u_{n_{un}} < u_{cp} \\ \dfrac{1}{1 + 0.45(u'_{n_{rec}})^{0.2}} & \text{for} \quad u_{n_{un}} \geq u_{cp} \end{cases} \tag{37}$$

is the damage factor correlated to the normalized recovery displacement $u_{n_{rec}} = u_{n_{un}} - u_{n_{ro}}$, as illustrated in Fig. 5(B). The coefficients following the normalized recovery displacement are calibrated with acceptable accuracy based on the experimental data gathered from the literature [51–53,59,60].

2.4. Stress update in explicit integration scheme

Oktiovan et al. [12] highlighted that proper handling of the force (or stress) update routine when the stress state violates the yield surface is essential to ensure the stability of the explicit time-marching integration system. In contrast to the typical stress update routine in an implicit-based solver, e.g., return mapping [16,61] or substepping [18,24], the stress update in the explicit integration scheme is relatively straightforward. This stress update routine is illustrated in Fig. 6(A) when each failure surface in the proposed constitutive model is violated.

From time t to $t+1$, the stress state progresses either linearly through the increments in Eq. (12), or through hardening for the normal compressive stress in Eq. (22). When F_1 is violated at time $t+1$ (circle marker in Fig. 6(A)), only the normal stress component σ_n of the stress state σ is corrected to the current tensile strength that is weakened through Eq. (17). This is because damage in Mode-I fracture reduces the normal capacity, while shear components remain unaffected at the instant of pure tensile failure. This is done to avoid introducing artificial shear when the joint opens and to respect the unilateral contact (i.e., no traction in tension once the cut-off line is reached). Note that this force correction occurs at the same time step $t+1$, where the failure surface is violated.

When F_2 is violated (triangle marker in Fig. 6(A)), the shear stress components in all directions are corrected to the weakened shear stress defined in Eq. (18). However, the force correction is scaled proportionally through Eq. (38). This choice is frame-invariant in the tangential plane and acts as a closest-point projection in the shear subspace. The normal component is unchanged because shear strength is the active limiter.

$$\boldsymbol{\tau}^{\mathbf{s}} = \boldsymbol{\tau}^{\mathbf{s}} \frac{\boldsymbol{\tau}^{\mathbf{s}}(d_{ts})}{\|\boldsymbol{\tau}^{\mathbf{s}}\|} \tag{38}$$

When the compression or shear–compression mode in F_3 is violated, as illustrated by the square marker in Fig. 6(A), both the normal and shear stresses are corrected through a radial return from the origin to the weakened cap. This is done by taking the radius from the point of origin (zero normal and shear stress), and correcting the stress state σ proportionally to the weakened normal compression and shear stresses through Eqs. (23) and (18), respectively. The correction amount is the radius difference between the violated stress state and the stress state at the weakened yield surface, termed **R** in Fig. 6(A), which has the same structure as σ. The correction for F_3 is formally defined as follows.

$$\left(\sigma^{t+1}\right)_1 := \left(\sigma^{t+1}\right)_1 - (\mathbf{R})_1, \qquad \left(\sigma^{t+1}\right)_{2:4} := \left(\sigma^{t+1}\right)_{2:4} \frac{(\mathbf{R})_{2:4}}{\left|\left(\sigma^{t+1}\right)_{2:4}\right|} \tag{39}$$

This choice yields a unique, path-independent correction that drives the yield function to zero in a single step and captures the coupled nature

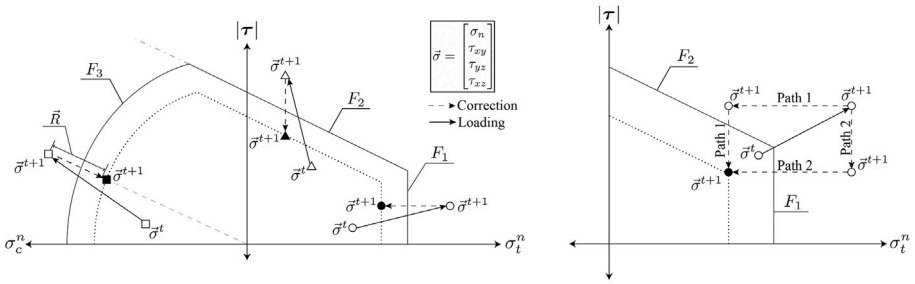

Fig. 6. Stress update on the interface once the failure surface is violated.

of shear–compression failure. As pointed out by Nie et al. [16], problems with multi-surface plasticity models arise when the updated stress is located close to a corner, i.e., the intersection between F_1 and F_2 and between F_2 and F_3 in the case of Fig. 6(A). This approach implements a general solution [20], as illustrated in Fig. 6(B) when both tensile cutoff F_1 and Coulomb friction line F_2 are violated. Two sequential stress correction paths are computed and compared at the intersection of $F_1 \cap F_2$. Path 1 first corrects the tension condition, then corrects the shear stress to satisfy the F_2 line. Path 2 first reduces the shear stress on F_2, then applies the secondary correction to meet F_1. Each path yields a candidate at the intersection corner. The active path is determined by the trigger order; the surface violated first in the current increment is selected as the candidate. This tie–break rule yields a unique update, preserves non-negative dissipation, and prevents oscillation between surfaces in subsequent steps.

2.5. Numerical implementation of the joint constitutive model

The joint constitutive model for analysing masonry structures using the Distinct Element Method (DEM) is implemented in *3DEC* [41]. The numerical treatment of cyclic loading, unloading, and reloading in the normal direction is detailed in the Appendix. Due to the dynamic nature of the explicit time-marching scheme, unbalanced forces may fluctuate throughout the simulation, particularly in response to changes in contact, local perturbations, or insufficient damping. If not adequately controlled, these fluctuations may be misinterpreted by the cyclic constitutive law, formulated in terms of displacement increments, as spurious loading and unloading events, which can result in artificial damage accumulation or instability in the material response. To mitigate this issue, a fail-safe perturbation flag is introduced for compression-side unloading, as described in A and implemented in the presented algorithm. The flag gates the transition to the unloading branch: the model enters unloading only when a genuine reversal out of compression is detected, rather than a transient oscillation. While the response is flagged as fluctuating, the normal contact is held at its initial elastic stiffness, preventing premature stiffness degradation and preserving the stability of the response.

In contrast, the shear response follows a simpler scheme, governed by a linear elastic unloading mechanism. Furthermore, historical parameters are incorporated into the damage scalars in tension d_t, shear d_s, and compression d_c to ensure consistent damage tracking under load reversals. This allows the model to retain and apply the maximum recorded value of relevant quantities, such as displacements or stresses, regardless of the current loading direction.

3. Material-level validation

A series of material characterization tests was conducted to validate the proposed joint constitutive model, utilizing cyclic loading protocols. The material-level validations serve to highlight the capability of the modelling strategy to simulate the failure of masonry constituents in shear, compression, as well as the dilatancy weakening effect on the overall response of the masonry assemblage. To that end, the cyclic uniaxial compression test conducted as part of the experimental campaign by Esposito et al. [62], the cyclic direct shear test on masonry assemblage by Atkinson et al. [50], and the masonry triplet test by Andreotti et al. [13] were selected as the validation cases. The tests by Esposito et al. [62] and Andreotti et al. [13] were conducted on calcium silicate masonry samples, while Atkinson et al. [50] conducted the test on clay brick samples. Table 1 summarizes the material properties used as input parameters in the selected material characterization tests.

The parameters include normal and shear stiffnesses, strength characteristics in tension, shear, and compression regimes, the corresponding fracture energies, and the dilatancy-related values governing the mechanical response of the masonry components. Due to the rigid block formulation, where the deformability of the units is neglected, and their Young's modulus is not explicitly defined, the initial normal k^n and shear k_i^s stiffnesses must be calibrated to the initial stiffness of the experiments. Therefore, the initial stiffnesses are first defined through the homogenized equation by Lourenço [1] (Eq. 40), which are then calibrated to match the experimental initial stiffnesses.

$$k_n = \frac{E_b E_m}{t_m \left(E_b - E_m\right)}, \qquad k_s = \frac{G_b G_m}{t_m \left(G_b - G_m\right)} \tag{40}$$

where E_b and E_m are the brick's and mortar's Young's moduli, respectively, G_b and G_m are the brick's and mortar's shear moduli, respectively, and t_m is the mortar joint thickness.

The cohesion c and friction angle ϕ were obtained from direct-shear/couplet tests based on the relation of $\tau = c + \sigma_n \tan\phi$ for all test cases. The residual cohesion c_{res} was read from the large-slip plateau. The initial dilation angle ψ is taken from the peak dilation observed in the direct shear test by Andreotti et al. [13]. The other parameters related to the dilatancy softening (i.e., $u^{s,\max}, \delta$ are refined according to the experimental findings). The tensile/bond strength f_t was taken from the companion splitting/bond tests, which are recalibrated to align the simulated peak load with the average measured response of the test cases. This recalibration is done using the empirically-derived equations summarized by Jafari et al. [63] . The mode-I G_I and mode-II G_{II} fracture energies are taken from the empirical equation set by CEB-FIP Model Code 90 [64]. The compressive strength f_t and the fracture energy G_c for the cyclic compression tests were taken from the experimentally reported values in Esposito et al. [62] . The hardening factor n for compressive strength was defined according to the recommendations of Jafari et al. [63] . This tailored parameter set provides a robust foundation for accurately simulating and validating the mechanical behavior of masonry under cyclic loading.

Fig. 7 presents the geometries and the loading configurations of the selected material characterization tests, with the extended dimensions of the brick units. The extended dimensions account for the thickness of the mortar layers while maintaining the actual height and width of the experimental specimens. The vertical and horizontal compression tests (Fig. 7(A) and Fig. 7(B), respectively) also include the locations of the

Table 1
Material properties used as the input parameters of the material characterization tests.

Material parameters	Symbol	Unit	Cyclic compression[1]		Cyclic shear-I[2]	Cyclic shear-II[3]
			Vertical	Horizontal		
Experimental parameters						
Density	ρ	kg m^{-3}	1800	1800	2300	1800
Peak cohesion	c_0	MPa	0.22	0.22	0.16	0.11
Residual cohesion	c_r	MPa	0.022	0.022	0.016	0.011
Friction at constant volume	ϕ_{cv}	∘	25.0	25.0	34.79	30.0
Initial dilatancy angle	ψ_0	∘	–	–	–	20.0
Compressive strength	f_c	MPa	6.5	7.45	–	–
Compressive fracture energy	G_c	N mm^{-1}	15	31.5	–	–
Numerical model parameters						
Normal stiffness	k^n	N mm^{-3}	52.1	52.1	9.17	32
Shear stiffness	k_i^s	N mm^{-3}	22.7	22.7	3.95	32
Tensile strength[4]	f_t	MPa	0.11	0.11	0.1	0.11
Hardening factor[4]	n	[-]	7.5	5.0	–	–
Zero dilation displacement	$u^{s,\max}$	mm	–	–	–	3.0
Dilatancy softening gradient	δ	[-]	–	–	–	2.0
Mode-I fracture energy[5]	G_I	N mm^{-1}	0.0086	0.0086	0.0081	0.00866
Mode-II fracture energy[5]	G_{II}	N mm^{-1}	0.0866	0.0866	0.081	0.0866
Cap parameters	C_n, C_{nn}, C_{ss}	[-]	0.0,1.0,12.0			

[1] Cyclic uniaxial compression test by Esposito et al. [62].
[2] Cyclic direct shear by Atkinson et al. [50].
[3] Cyclic triplet test by Andreotti et al. [13].
[4] Based on the recommendations by Jafari et al. [63].
[5] Values obtained from CEB-FIP Model Code 90 [64].

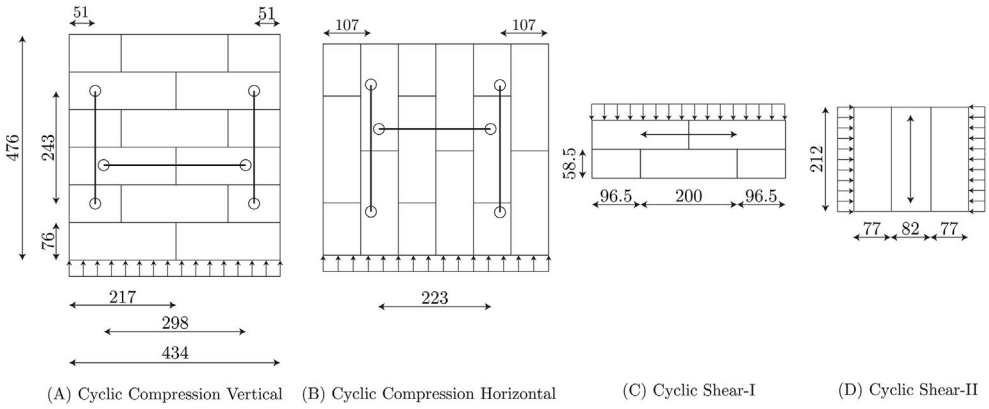

Fig. 7. Illustration of the validated material characterization tests with extended brick dimensions.

LVDTs used to record the axial strain. The axial strain in the numerical model is calculated from the relative displacement between the two vertical LVDTs on the front and back sides of the specimen.

3.1. Uniaxial cyclic compression tests

There are two configurations considered in the uniaxial compression test: a vertical configuration, where the compression load is orthogonal to the bed joints, and a horizontal configuration, where the compression load is orthogonal to the head joints. Similar to the experiment, the displacement-controlled load is applied at the bottom of the model using a rigid plate, with the stresses recorded at the top of the prisms [62]. Due to the brittle post-peak response, the experimental cyclic unloading/reloading scheme was only performed during the pre-peak phase. The unloading/reloading scheme was conducted three times at the 25 %, 50 %, and 75 % of the peak compressive stress.

The comparison of the uniaxial cyclic compression test on the vertical and horizontal prisms is presented in Fig. 8. Two results were shown as the cyclic loading experiment was conducted twice, to highlight the variability in mechanical response. Despite being cast from the same batch, the specimens responded differently, indicating non-negligible experimental variability or inherent material heterogeneity. However, the model was tuned to one specific specimen, TUD-MAT-11G for the vertical case, and TUD-MAT-11K for the horizontal case.

By employing the nonlinear unloading scheme in Eq. (31), the model effectively captured the energy dissipation observed during unloading and reloading in both vertical and horizontal prism tests. It reproduced key hysteretic behaviors such as stiffness degradation and residual strains, demonstrating its ability to simulate the cyclic compressive response of masonry-like materials with directional consistency. Furthermore, the behavior where the reloading strain exceeded the unloading onset was also evident in both vertical and horizontal cases, which were consistently simulated by the proposed joint constitutive model.

3.2. Cyclic direct shear test on masonry bed joints

Atkinson et al. [50] conducted cyclic shear tests on masonry assemblages with old and new clay masonry units with mortar joint thicknesses of 7 and 13 mm. The old clay assemblage was tested under a pre-compression level of 13 kN while the new clay assemblage was tested under 49 kN of pre-compression force. In this experiment, the top-side loading plate was sheared up to 12 mm before the specimen was unloaded and then loaded in the other direction.

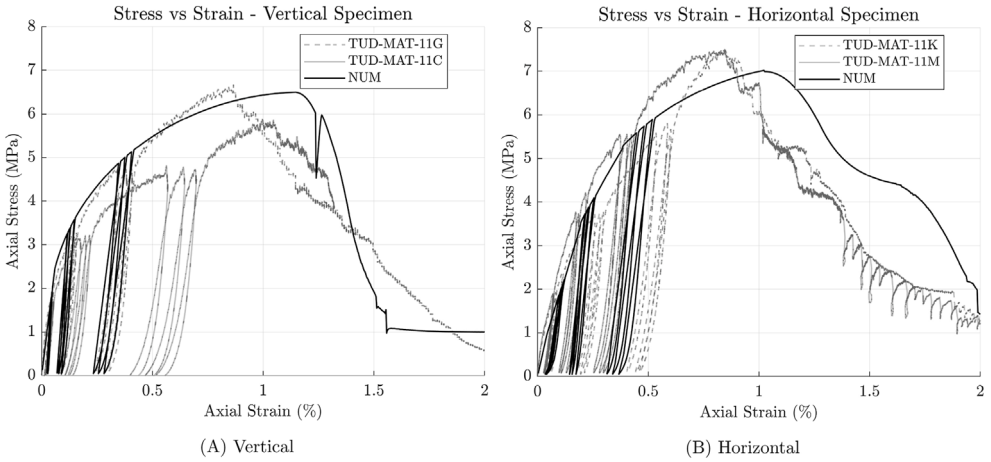

Fig. 8. Uniaxial compression test results comparison.

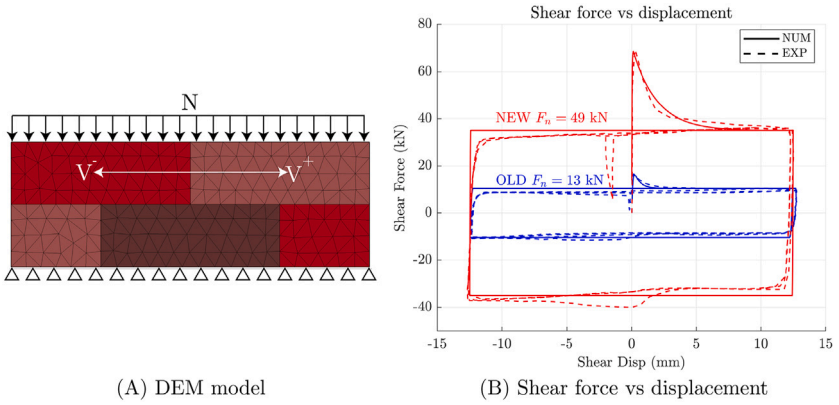

Fig. 9. The DEM model with the boundary conditions and the comparison to experimental results.

For both pre-compression levels reported by Atkinson et al. [50], a single set of interface parameters in Table 1 was used, and only the applied normal force was varied, so that differences in the simulated response reflect confinement effects rather than parameter changes. The DEM model and the boundary conditions are shown in Fig. 9(A), where the bottom units are fixed, and precompression is applied directly to the top units, along with the cyclic shear load. The shear force–displacement comparison is presented in Fig. 9(B).

The numerically predicted responses closely reproduce the overall experimental behavior, accurately capturing key response features such as the initial stiffness, peak shear strength, post-peak mode-II softening, and the elastic unloading/reloading branch typical of shear, as well as the residual strength plateau for both normal stress conditions.

3.3. Cyclic shear test on masonry triplet

The dilatant behavior of masonry joints subjected to combined shear and compressive loads was experimentally investigated by Andreotti et al. [13]. The test setup adopted in their study is illustrated in Fig. 10(A). The test was conducted on calcium-silicate brick specimens with the dimensions of $212 \times 102 \times 72$ mm and mortar layers with the thickness of 10 mm. The pre-compression force actuator was controlled through a spring with a stiffness of $1070\,\mathrm{N\,mm^{-1}}$ to regulate and maintain the desired pre-compression level (N). The shear force is applied through a vertical jack, and the rotation of the whole triplet is not restricted. The triplet was subjected to three time windows, defined by the sequential application of the shear load, but with an increasing precompression level at each time window. In each window, the shear force is characterized by loading and complete unloading to a zero shear force condition. Time window zero refers to the shear test of a pristine triplet, while the subsequent time windows are conducted to find the residual shear strength corresponding to the constant volume phase. Readers are referred to Andreotti et al. [13] for further details pertaining to the experimental procedure.

The numerical model follows the configuration and procedure of the experimental tests as closely as possible, illustrated in Fig. 10(B). In the experiments, the axial load was held within three time windows by a spring-regulated actuator (force-controlled target with finite actuator stiffness), not by an unconstrained constant-force device. This maintains the prescribed pre-compression while allowing the normal force to react to specimen dilation. In the model, this is reproduced by a simple servo/spring control, where, given a target displacement set at each time window, the model calculates the relative displacement between the triplet's volumetric expansion and the target displacement and transfers that as an applied force to the steel plate, allowing the normal precompression force to be adjusted according to the volumetric expansion. This is formally expressed as:

$$F(t) = K_{act}\left[u_{cmd}(t) - u_{spec}(t)\right] \tag{41}$$

where K_{act} is the actuator stiffness, set at $1070\,\mathrm{N\,mm^{-1}}$, $u_{cmd}(t)$ is the commanded actuator displacement (target) and the $u_{spec}(t)$ is the measured specimen-side displacement at the actuator interface.

Leveraging the conditional stability of the explicit solver, the simulation of the triplet test is performed sequentially from one time window

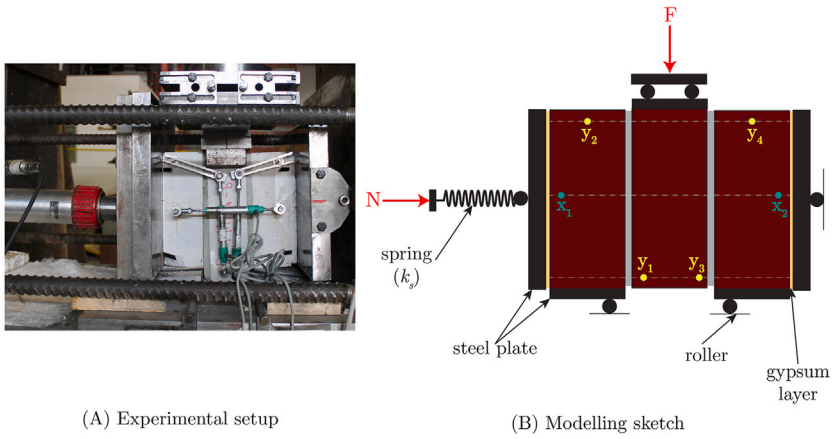

Fig. 10. Experimental setup [13] and the boundary conditions of the DEM model.

to another using the same material properties and boundary conditions from the previous window, consistent with the experimental procedure. The shear displacement ($u_{s,rel}$) and the volumetric expansion ($u_{n,rel}$) are calculated according to Eqs. (42) and (43), respectively, averaged on the front and back sides of the specimen [13].

$$u_{s,rel} = \frac{y_1 - y_2}{y_3 - y_4} \tag{42}$$

$$u_{n,rel} = x_2 - x_1 \tag{43}$$

The responses from the proposed modelling strategy (shown in solid lines) are compared to the experimental data (dashed lines) of the triplet test in Fig. 11. In time window 0 (displayed in blue), the numerical model exhibited the exponential softening response where the shear stress decayed to a residual value of 0.2 MPa (Fig. 11(A)), while the normal stress initially increased due to volumetric expansion but remained constant at the same level as the experimental test (Fig. 11(B)). The gradual decline of the experimental shear stress is explained by the sequential failure of the mortar joints: cracking initiated in the left-hand joint of Fig. 10(B) and subsequently propagated to the right-hand joint, progressively diminishing the overall shear-carrying capacity. The volumetric expansion (Fig. 11(C)) was also in good agreement with the experimental observation, where the exponential volumetric expansion due to the normal displacement correction in Eq. (27) is evident in the numerical response. From the comparison of the dilatancy coefficient in Fig. 11(D), the experimental results showed that the coefficient dropped to zero beyond the shear displacement of 2.0 mm, which was consistently modeled by the exponential decay function in Eq. (26).

At time window 1 (displayed in red), the shear stress, normal stress, and the dilatancy coefficient were in good agreement with the experimental data. However, the numerical responses were higher and more fluctuating compared to the experimental data. The uncontrolled volumetric expansion arose from the specimen's ability to rotate freely. When the pre-compression is increased abruptly, this unconstrained rotation interacts with the sudden confinement, triggering a rapid dilative response. At time window 2 (displayed in orange), the normal stress was elevated to 0.9 MPa, resulting in the shear stress of approximately 0.55 MPa. Thereafter, the joint again evolves toward a stable, slightly dilatant state, with the dilatancy coefficient fluctuating about zero as asperities are fully smoothened at this state.

Overall, the proposed modelling strategy reproduced the dilatancy behavior observed in the triplet test with good fidelity. Across all windows, the numerical solution tracks well the measured trends, capturing the stress jumps, the progressive reduction of dilatancy, and the ultimate approach to steady-state shear and volumetric response, lending confidence to the implemented constitutive formulation. The specimen was chosen to span the representative failure modes (cracking, shearing, and crushing) as well as mixed-mode combinations and transitions between them, ensuring that the assessment probed the model across the full spectrum of observed responses.

4. Structural-level validation

In this section, the proposed modelling strategy is validated using four single-wythe calcium silicate (CS) masonry walls subjected to constant compression and cyclic in-plane loading, as reported in the experimental campaign conducted by Messali et al. [65]. The test matrix was designed to isolate the effects of boundary restraint and aspect ratio. Two wall geometries, squat and slender, were evaluated under both cantilever and double-clamped end conditions, yielding four representative specimens. The assessment draws on both global responses, force–displacement hysteresis and energy dissipated per cycle, and local responses, specifically the evolution of crack patterns.

4.1. Geometrical and material properties

The experimental setup of the reference case is presented in Fig. 12. The vertical compression load is applied as a uniform pressure through the four actuators placed on top of the steel beam, while the displacement-controlled load is applied through one actuator at the top of the walls. The upper and bottom courses of the wall were glued to the steel beams to prevent sliding or tensile cracks at the steel beam-to-masonry interface. The out-of-plane movement and rotation of the top beam were restricted through a steel frame, as presented in the A-A' section in Fig. 12(B). The colors inside the bricks are for visualization only (no material heterogeneity is implied). The top and bottom beams were clamped for the double-clamped configuration (grey elements), while only the bottom side was clamped on the cantilever configuration. The walls were allowed to move vertically, thereby maintaining a constant applied pre-compression load. The geometrical properties and the reported failure mechanism are presented in Table 2.

A single set of material properties is used for all validated specimens, as summarized in Table 3. The material properties, such as the unit's Young's modulus, Poisson's ratio, and density, as well as mortar compressive strength and masonry compressive strength, are obtained through the material characterization tests conducted before the quasi-static wall experiment (see the full report by Esposito et al. [62]). Meanwhile, properties such as the mortar modulus of elasticity and the peak ratio n are obtained from empirical equations reported in Jafari et al. [42] . The unit-mortar interface properties, such as tensile and cohesive strengths, as well as the normal and shear stiffnesses, are calibrated to match the numerical force–displacement curves with the experimental envelope curves.

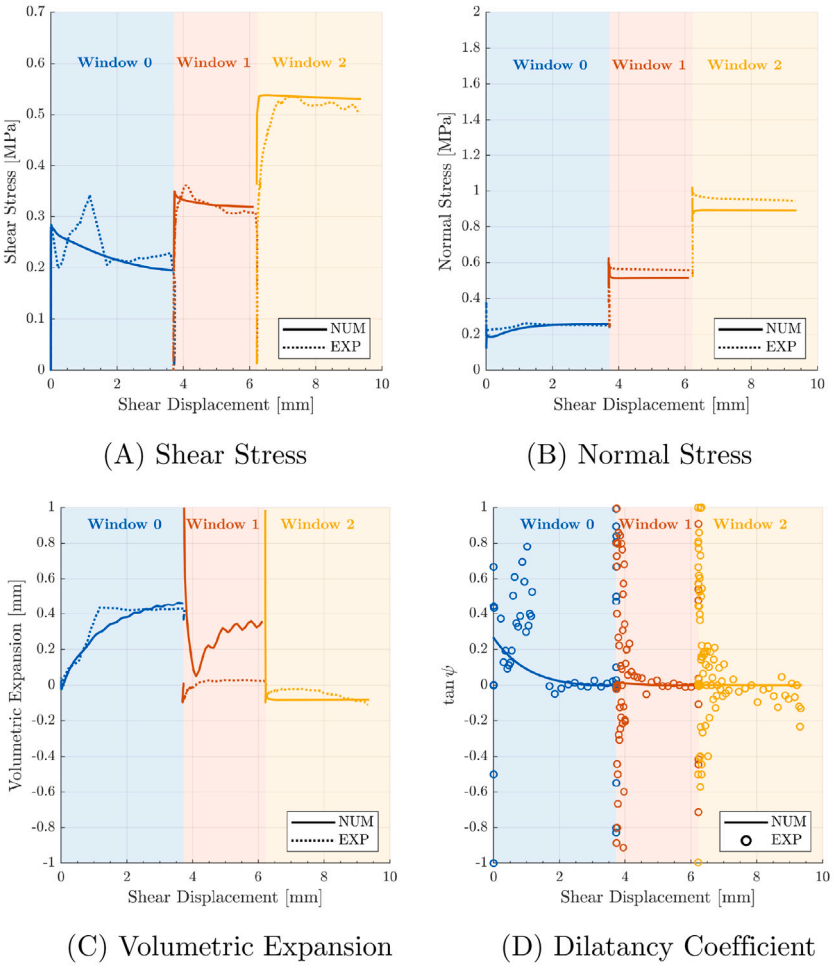

Fig. 11. Validation of the modelling strategy to a triplet test on multiple time windows [13].

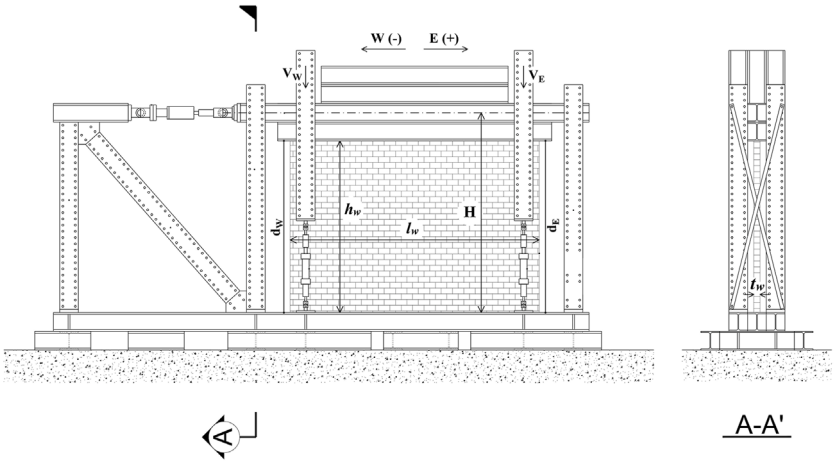

Fig. 12. Experimental setup of the in-plane test on CS masonry wall [65].

4.2. Modelling setup

The brick discretization of the representative models (slender, double-clamped on TUD-COMP-0a (Fig. 13(A))) and squat, cantilever on TUD-COMP-6 (Fig. 13(B)) is presented in Fig. 13. The loads and supports in the numerical model are applied through blocks with a high Young's modulus (grey-colored blocks in Fig. 13, which are perfectly connected to the masonry blocks. The blocks are defined in a rigid block configuration, with potential crack surfaces placed at the mid-length of the brick units.

For the walls with cantilever configuration (TUD-COMP-1 and TUD-COMP-6), the in-plane rotation of the top block is free, and the block height is extended up to the point where zero moment is observed according to the wall shear ratio reported in Table 2. This ensures the

Table 2
Geometrical properties of validated wall specimens (Messali et al. [65]).

Specimen name	Dimensions [m] $l_w \times h_w \times t_w$	Shear ratio	Boundary conditions	Vertical pre-compression [MPa]	Failure mode
TUD-COMP-0a	1.1 × 2.76 × 0.102	1.25	Double clamped	0.70	Rocking-sliding
TUD-COMP-1	1.1 × 2.76 × 0.102	2.90	Cantilever	0.70	Rocking
TUD-COMP-4	4.0 × 2.76 × 0.102	0.35	Double clamped	0.50	Diagonal shear
TUD-COMP-6	4.0 × 2.76 × 0.102	0.80	Cantilever	0.50	Diagonal shear + crushing

Table 3
Material properties of the calcium silicate masonry walls.

Properties	Symbol	Unit	Value	
Unit properties				
Density	ρ	kg m^{-3}	1800	
Interface properties			Bed joint	Head joint
Masonry modulus of elasticity[a]	E	MPa	3174.6	3174.6
Mortar modulus of elasticity[b]	E_m	MPa	1973.72	
Normal stiffness[c]	k^n	GPa m^{-1}	52.17	52.17
Shear stiffness[c]	k^s	GPa m^{-1}	22.49	22.49
Tensile strength[c]	f_t	MPa	0.105	0.035
Cohesive strength[c]	f_s	MPa	0.14	0.014
Friction coefficient[a]	μ	[-]	0.466	
Mode-I fracture energy[a]	G_I	N m^{-1}	8.38	3.88
Mode-II fracture energy[a]	G_{II}	N m^{-1}	83.8	38.8
Compressive strength[a]	f_c	MPa	5.93	7.0
Compressive fracture energy[a]	G_c	N m^{-1}	15,000	31,500
Peak ratio[c]	n	[-]	7.5	
Cap parameters	C_n, C_{nn}, C_{ss}	[-]	0.0,1.0,12.0	

[a] Values obtained from material characterization tests in Esposito, et al. [62].
[b] Values derived from equations reported in Jafari et al. [42].
[c] Evidence-backed input parameters.

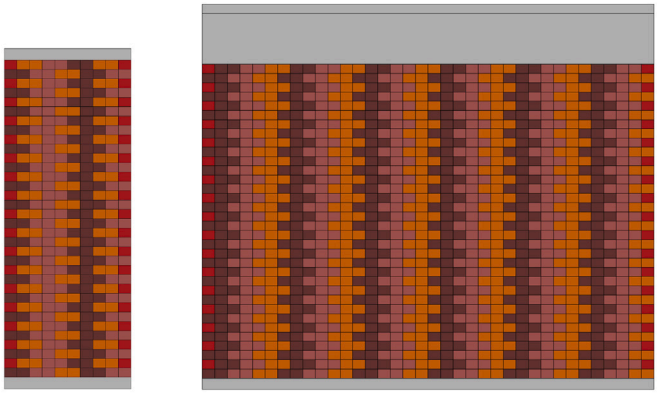

(A) TUD-COMP-0a (B) TUD-COMP-6

Fig. 13. Representative model of the CS wall in *3DEC*.

applied in-plane load imposes the correct moment at the wall base. For the walls with a double-clamped configuration (TUD-COMP-0a and TUD-COMP-4), the in-plane rotation of the top block is fixed, and its height is set equal to that of the bottom block, as the location of the applied load is irrelevant in this configuration.

The model is first brought to equilibrium under gravity load, which is then followed by the application of the pre-compression load. The equilibrium under an explicit integration scheme is quantified through the ratio of the remaining out-of-balance force components to the total forces applied to every node [12]. In this paper, the equilibrium is assumed to be reached when the ratio is less than 1×10^{-5}. Local numerical damping is used throughout the simulations, with the damping factor α (Eq. 9) set to 0.8 by default.

To minimize the inertial overshoot during load reversal, the cyclic load is applied as a sequence of impulse pulses. The cosine-plateau-cosine velocity history is mathematically defined in Eq. (44), which concentrates the entire prescribed displacement u_{apv}, within the finite time span of $t_{tot} = 2t_a + t_b$.

$$V(t) = \begin{cases} \dfrac{v_{max}}{2}\left[1 - \cos\left(\dfrac{\pi t}{t_a}\right)\right], & 0 \le t < t_a, \\ v_{max}, & t_a \le t < t_a + t_b, \\ \dfrac{v_{max}}{2}\left[1 + \cos\left(\pi(t - t_a - t_b)/t_a\right)\right], & t_a + t_b \le t < t_{tot}, \\ 0, & t \ge t_{tot} \end{cases} \tag{44}$$

where $t_a = 0.5d_d$, $t_b = d_d * \kappa$, κ is the dimensionless parameter that defines how long the constant-velocity plateau should last compared to the cosine ramp up and down, and d_d is the ramp duration correlated to the prescribed displacement u_{apv}, maximum velocity v_{max}, and plateau factor κ, as defined in Eq. (45). In all simulations described in Section 4, the applied loading velocity is set to 5.0 mm s^{-1} and the plateau factor is set to 20 %.

$$d_d = \frac{u_{apv}}{v_{max}(1+\kappa)} \tag{45}$$

The impulse velocity in Eq. (44) is illustrated in Fig. 14 for a target displacement of 10 mm, an applied maximum velocity of 5 mm s^{-1}, and a mechanical timestep of 1×10^{-6} s. Fig. 14(A) shows the imposed velocity $v(t)$: a half-cosine ramp-up, a constant velocity plateau set at 5 mm s^{-1}, and a half-cosine ramp-down to zero (dashed lines mark the transitions). The smooth ramps avoid numerical spikes at mode switches. Let t_a be the duration of each ramp and t_b be the plateau duration. The resulting displacement in Fig. 14(B) is then calculated as:

$$u_{tar} = \int_0^{2t_a+t_b} v(t)\,\mathrm{d}t = v_{max}(t_a + t_b), \tag{46}$$

where u_{tar} is the target prescribed displacement. It can be seen that the resulting displacement in u_{tar} matches the target prescribed displacement of 10 mm.

This velocity profile is advantageous for cyclic loading in the explicit scheme, as the smoothness of the profile limits the artificial stress waves and dynamic amplification that can arise when a constant velocity load is applied to the system. The constant velocity plateau occurs when the system moves at a constant velocity, reaching the prescribed displacement faster while maintaining a kinetic energy level below the internal energy stored in the block system. This isolates the hysteretic response to reflect only the masonry non-linearities, rather than the system's inertia.

4.3. Validation results

This section evaluates the capability of the proposed modelling strategy against the experimental campaign at the component scale. The comparison is performed at both global and local levels, focusing on the reproduction of force-deformation characteristics, hysteretic behavior, and key damage mechanisms observed during the cyclic loading. Emphasis is placed on assessing the model's ability to capture stiffness degradation, strength evolution, and energy dissipation across different wall typologies.

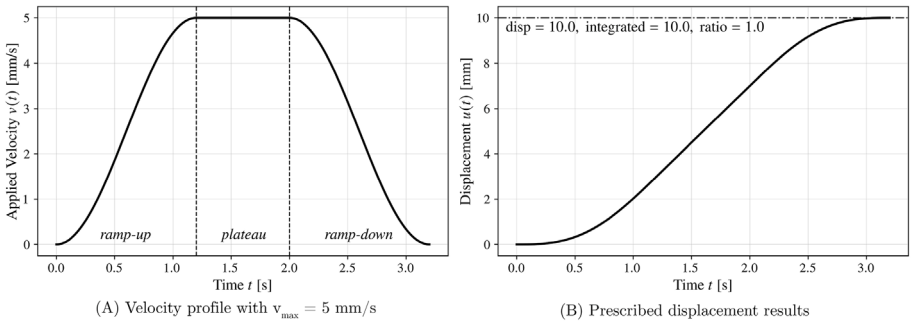

Fig. 14. Imposed actuator velocity profile $v(t)$ with v_{max} of 5 mm s^{-1} and the resulting displacement.

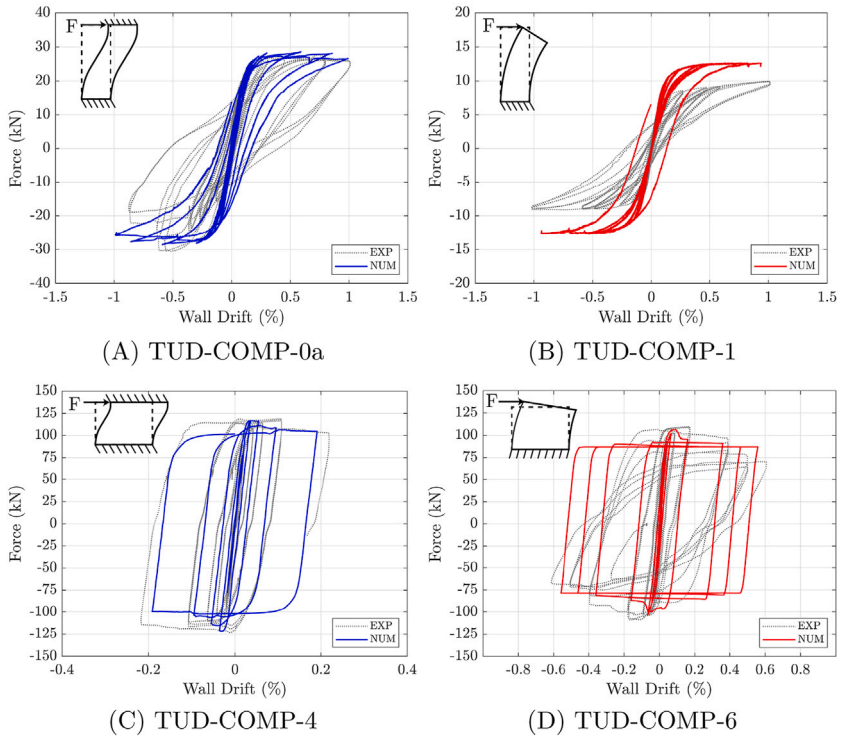

Fig. 15. Force-displacement results of all validated cases.

4.3.1. Global response - force-displacement curve and hysteresis performance

The lateral force-wall drift responses of the four walls predicted by the proposed modelling strategy are compared to the experimental responses in Fig. 15. For the slender cases, the TUD-COMP-0a (Fig. 15(A)) model predicted a symmetric response between the positive and negative loading cycles, matching the peak resistance of 28 kN and the softened post-peak branch, even though the hysteresis response was more pinched compared to the experimental curve at wall drifts beyond ±0.5%.

Compared to the experiment, TUD-COMP-1 (Fig. 15(B)) shows a higher simulated peak (12.5 kN compared to 10 kN in EXP, i.e., 25 % overestimation). The model also exhibited a more pinched hysteresis loop than the experimental observation. This discrepancy arises because the simulation remains rocking-controlled over a longer interval, and the sliding and shear–compression failure activates later than in the tests, reducing re-closure forces and increasing the apparent pinching. Furthermore, it is essential to emphasize that the simulation is done with a single interface parameter set for all four walls, which avoids specimen-by-specimen tuning but leaves some spread in peak and loop shape for the slender cantilever. Notably, the experimental report in Messali et al. [65] also reported that preliminary numerical analyses struggled with TUD-COMP-1, underscoring the difficulty of this configuration.

Nevertheless, in both slender cases, it is clear that rocking occurred during earlier loading cycles. In particular, the first few cycles in both TUD-COMP-0a and TUD-COMP-1 returned almost to the origin, indicating negligible permanent drift. As the imposed displacement increased, horizontal sliding along the bed-joint interface became mobilised, leading to progressively larger residual deformations that are faithfully reproduced by the numerical model.

For the squat specimens, TUD-COMP-4 (Fig. 15(C)) and TUD-COMP-6 (Fig. 15(D)), the numerical model reproduced the characteristic larger hysteresis loops that arose from shear-dominated behavior. In TUD-COMP-4 with the double-clamped configuration, the simulated envelope closely followed the experimental backbone, matching the experimental initial stiffness and the peak strength of approximately 125 kN. The model, however, exhibited a slightly faster drop in shear capacity compared to the experimental behavior after peak capacity was observed. For the cantilever model in TUD-COMP-6, where multiple

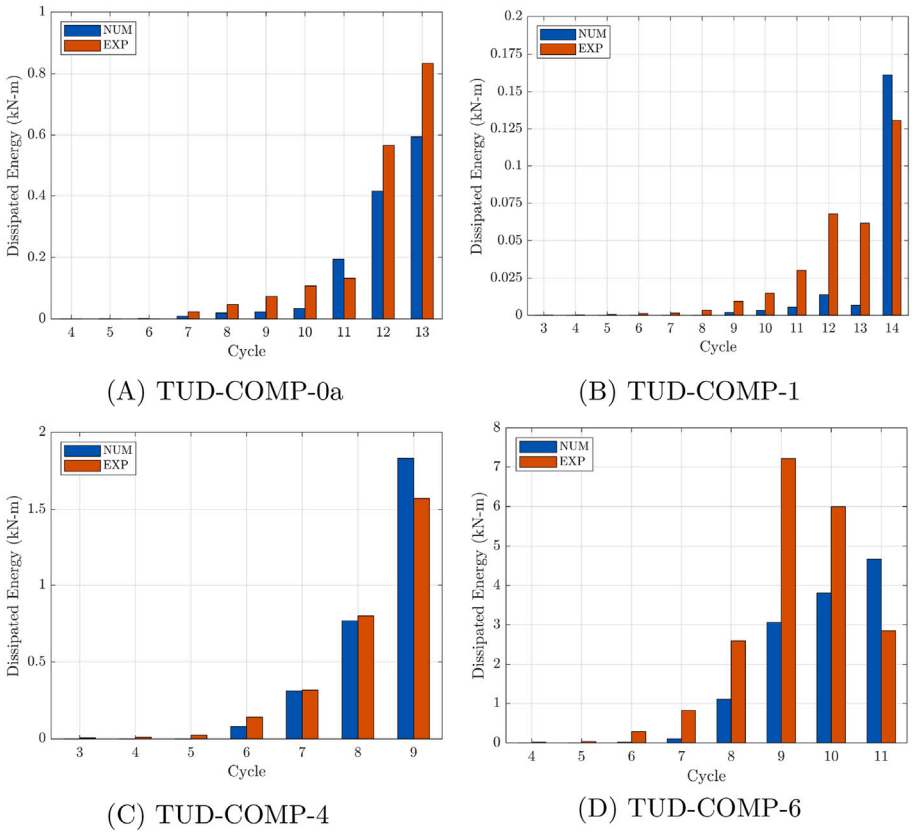

Fig. 16. Dissipated energy comparison of all validated cases.

diagonal cracks were observed during testing, the model captured the peak capacity relatively well at approximately 110 kN, but the hysteresis loops exhibited a more plastic response compared to the experiment, a typical behavior of a shear-dominated failure. Despite these differences, the simulation accurately reproduced the progressive strength degradation at large drifts and the symmetric response under cyclic loading, demonstrating that the proposed interface-shear formulation is robust for both squat walls and the more slender configurations discussed above.

Fig. 16 compares the dissipated energy in each relevant loading cycle as measured in the tests (shown in orange) with that computed by the numerical models (shown in blue) for the four benchmark walls. The relevant cycles are defined as the cycles in which the experimental curve exhibits hysteretic behavior. For the two slender walls, TUD-COMP-0a and TUD-COMP-1 (Fig. 16(A) and Fig. 16(B), respectively), the dissipated energy remains modest, never exceeding 1 kN m, as the response is primarily governed by rocking with sliding only in the later cycles. The model faithfully tracks the growth in energy with increasing drift, slightly over-predicting the dissipated energy in the last two cycles, which is consistent with the relatively more pinched hysteresis loops observed in the force–drift curves (Fig. 15(A) and Fig. 15(B)).

A considerably different behavior emerges for the squat specimens. In TUD-COMP-4 (Fig. 16(C)), once the diagonal cracking is activated, the dissipated energy significantly increases, ultimately reaching approximately 1.8 kN m in the final cycle. The model matches this increase, and the individual cycle-to-cycle values are comparable to the experimental response, with only slight over-estimation at the last cycle. The trend intensifies in TUD-COMP-6 (Fig. 16(D)), where shear-dominated behavior, coupled with toe crushing, yields a peak of 7 kN m at cycle 9, followed by a slight decline as strength degradation occurs. The model also reproduces the rapid build-up and the subsequent drop of dissipated energy, but it underestimates the single cycle carrying the maximum dissipation, consistent with the abrupt unloading observed in the force–drift curve in Fig. 15(D).

Overall, the comparison confirms that the proposed modelling strategy reproduces the global hysteretic behavior observed in the tests across the full spectrum of wall aspect ratios. It predicts the correct strength staircase and mirrors the progressive accumulation of energy dissipation as damage localizes. Although discrepancies remain in individual cycles, the numerical envelopes, stiffness degradation, pinching intensity, and cumulative energy trends all align closely with the experimental evidence, demonstrating the model's ability to provide reliable, system-level forecasts of masonry wall performance under cyclic loading.

4.3.2. *Local response - crack patterns*

Fig. 17 shows the experimentally mapped cracks at the end of the loading sequence, compared against the predicted joint damage scalar d_{ts} Eq. (21) for the two slender specimens. For TUD-COMP-0a (Fig. 17(A), the experiment developed symmetric rocking hinges at the upper and lower corners, manifested as stepped bed- and head-joint cracking. The simulation captures the same mechanism: d_{ts} localizes in stepwise bands at each corner, consistent with uplift-driven tensile failure as the compression toe migrates under cyclic loading. The model also reproduces the complete degradation of the top and bottom bed joints associated with hinge formation. The compressive damage field (Eq. (B.25)(A)) corroborates localized toe crushing at each corner.

For the cantilever model in TUD-COMP-1 (Fig. 17(B)), the experimental crack pattern exhibited a fan-shaped crack network starting from the base toward the mid-height, indicating a transition from pure rocking to combined rocking-sliding as the axial load was progressively

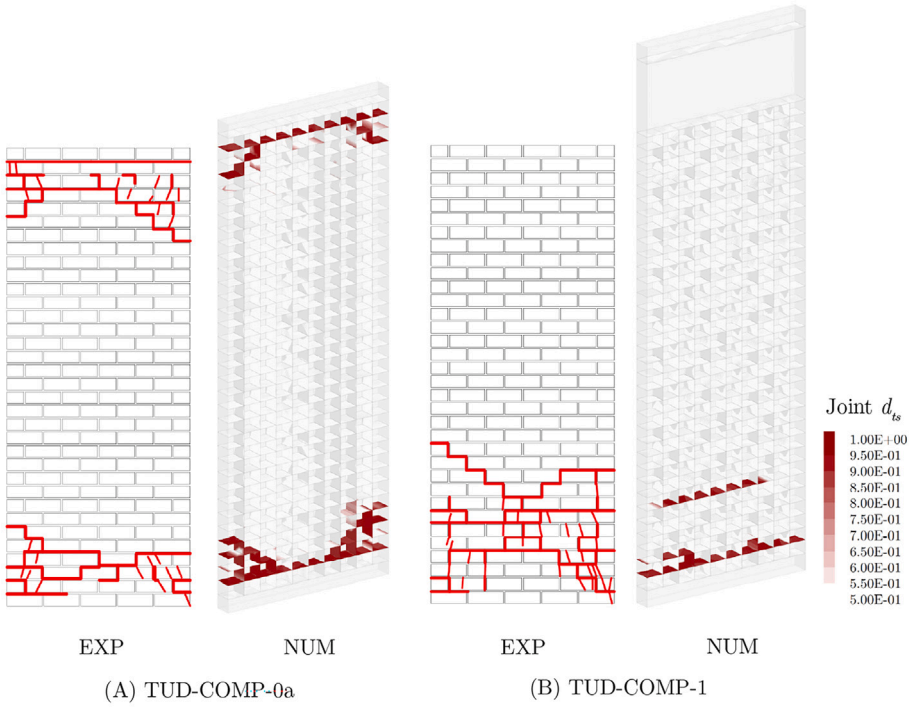

Fig. 17. The comparison of the experimental crack pattern to the combined d_{ts} damage scalar for the slender wall cases.

transferred to the compression side. The numerical model reproduced the horizontal slip line along the first bed joint from the base and the subsequent stepped propagation to the next course, albeit with fewer head-joint fractures, a difference attributed to the homogenized mechanical properties applied to the model. Nevertheless, the predicted failure mechanism is in good agreement with the experimental observation: a dominant sliding interface at the base, followed by splitting at the brick units, and diagonal cracks along the corners of the wall.

The crack pattern comparison for the squat wall specimens is presented in Fig. 18. The experimental crack pattern of TUD-COMP-4 (Fig. 18(A)) exhibits a typical X-shaped shear mechanism, with two diagonal cracks linking opposite corners and intersecting at mid-height. The numerical model reproduced this pattern significantly well, where both diagonals initiate from the same corners, converging at the wall's mid-height. Splitting of the brick units is also observed at the lower left corner of the wall.

The cantilever specimen of TUD-COMP-6 (Fig. 18(B)) showed a more intricate failure mode: the diagonal cracks formed first, followed by additional diagonal branches and partial horizontal slips at the top of the wall, which was then followed by the splitting of the brick units along the diagonal cracks. The numerical model captured these mechanisms relatively well, where diagonal cracks formed after partial horizontal slips occurred at the top of the wall. From the joint compression damage scalar plot in Fig. B.25(B), a small toe crushing zone was visible at each corner of the wall, coupled with the splitting of the brick units in Fig. 18(B). Although the numerical pattern showed somewhat fewer off-axis cracks compared to the experiment, the predicted locations and relative severities align relatively well with the experimental mapping. While the computational model captured fundamental local and global mechanisms observed during the testing, the performed deterministic analysis and adopted simplified micro-modelling strategy may yield less cracking within the brick domain; hence, inherently influencing the energy dissipation and macro-unloading stiffness of the analyzed URM wall.

Across both aspect ratios considered in this paper, the proposed modelling strategy consistently demonstrated the ability to capture the local damage mechanisms observed experimentally. Minor mismatches, such as slightly smoother crack trajectories or a lack of a stepwise crack pattern, were attributed to the homogenized mechanical properties implemented in the wall model. These findings confirm that the modelling strategy provides a robust, accurate, and detailed representation of damage in unreinforced masonry walls subjected to cyclic in-plane loading, regardless of whether the loading is dominated by rocking or shear.

5. Discussion

This section discusses the structural-level results by interpreting both the mechanical and numerical factors governing the observed cyclic response. First, the influence of local numerical damping on the predicted energy dissipation is examined to verify that the hysteretic behavior is dominated by physical mechanisms rather than numerical artefacts. Then, the discussion addresses the drift-dependent transition between in-plane failure mechanisms, followed by an assessment of the sensitivity to the imposed loading rate, and a comparison with alternative numerical approaches reported in the literature.

5.1. Influence of local numerical damping on energy dissipation

This section investigates the influence of local numerical damping on the energy dissipation mechanism for the benchmark case of TUD-COMP-0a, to verify that the simulated response is governed by physical dissipation mechanisms rather than by algorithmic stabilization effects. Given the known problem-dependence of numerical damping in explicit DEM analyses, such a verification step is essential before interpreting the mechanical response.

Let $S(t)$ be the set of active subcontacts included in the energy accounting (excluding subcontacts between the boundary blocks and masonry). All energy terms are expressed in Joules (N·m). For each subcontact s, the joint constitutive model evaluates energy contributions associated with normal and shear relative motion at the interface. These quantities represent the mechanical work performed by the corresponding tractions and are computed incrementally during the explicit time integration.

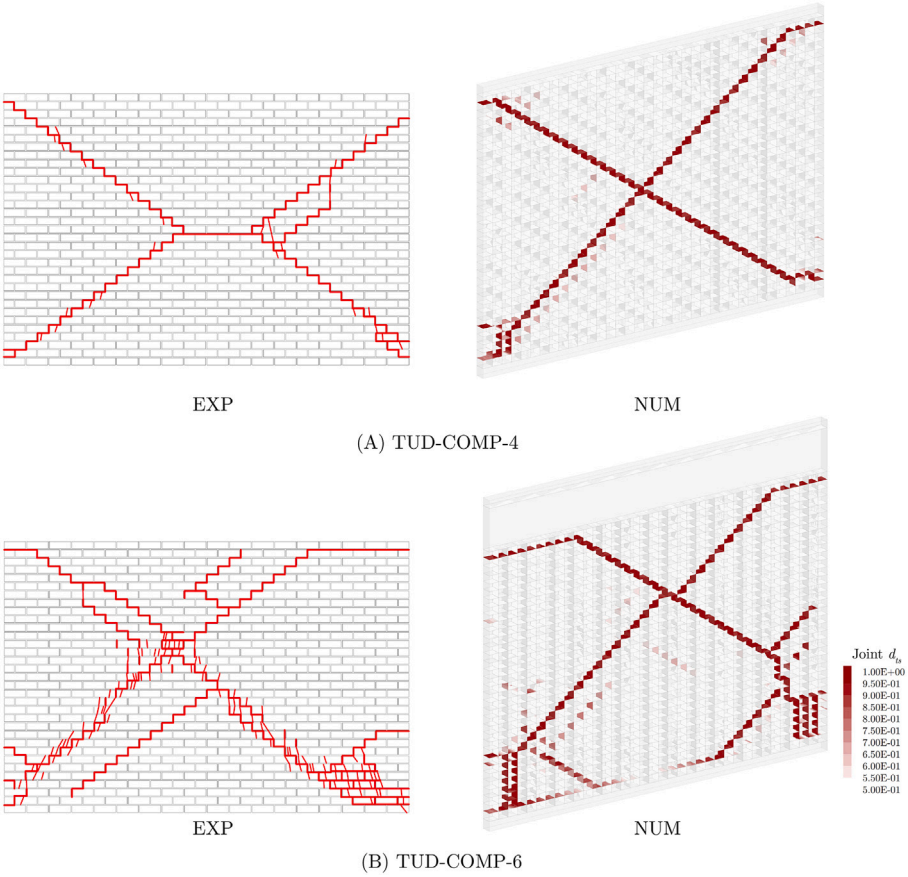

Fig. 18. The comparison of the experimental crack pattern to the combined d_{ts} damage scalar for the squat wall cases.

The normal tensile and compressive components are defined as:

$$E^{(s)}_{\text{tens}}(t) = \int_0^{u_t^{n,(s)}(t)} \langle T_n^{(s)} \rangle^+ \, \mathrm{d}u_t^{n,(s)}, \qquad E^{(s)}_{\text{comp}}(t) = \int_0^{u_c^{n,(s)}(t)} \langle -T_n^{(s)} \rangle^+ \, \mathrm{d}u_c^{n,(s)}, \tag{47}$$

where $T_n^{(s)}$ denotes the normal traction, $\mathrm{d}u_t^{n,(s)}$,$\mathrm{d}u_c^{n,(s)}$ are the incremental displacement in tension and compression, respectively. The shear energy is defined as:

$$E^{(s)}_{\text{shear}}(t) = \int_0^{\boldsymbol{u}_s^{(s)}(t)} \boldsymbol{T}_s^{(s)} \cdot \mathrm{d}\boldsymbol{u}_s^{(s)}, \tag{48}$$

where $\boldsymbol{T}_s^{(s)}$ is the shear traction vector. This contribution captures energy dissipation due to frictional sliding and shear-related inelastic mechanisms under cyclic loading.
The joint model then returns the instantaneous energy components as:

$$E_{\text{tens}}(t) = \sum_{s \in S(t)} E^{(s)}_{\text{tens}}(t), \tag{49}$$

$$E_{\text{comp}}(t) = \sum_{s \in S(t)} E^{(s)}_{\text{comp}}(t), \tag{50}$$

$$E_{\text{shear}}(t) = \sum_{s \in S(t)} E^{(s)}_{\text{shear}}(t), \tag{51}$$

At discrete times t_n, the dissipated energy for each component is calculated as:

$$E^{\text{diss}}_{\text{tens}}(t_N) = \sum_{n=1}^{N} \left| E_{\text{tens}}(t_n) - E_{\text{tens}}(t_{n-1}) \right|, \tag{52}$$

$$E^{\text{diss}}_{\text{comp}}(t_N) = \sum_{n=1}^{N} \left| E_{\text{comp}}(t_n) - E_{\text{comp}}(t_{n-1}) \right|, \tag{53}$$

$$E^{\text{diss}}_{\text{shear}}(t_N) = \sum_{n=1}^{N} \left| E_{\text{shear}}(t_n) - E_{\text{shear}}(t_{n-1}) \right|. \tag{54}$$

which are then combined to return the cumulative energy from physical dissipation $E_{\text{phys}}(t_N)$ as:

$$E_{\text{phys}}(t_N) = E^{\text{diss}}_{\text{tens}}(t_N) + E^{\text{diss}}_{\text{comp}}(t_N) + E^{\text{diss}}_{\text{shear}}(t_N) \tag{55}$$

Meanwhile, the cumulative work removed by local numerical damping, denoted by W_k, is evaluated at the block level from the unbalanced forces and translational velocities. At each timestep t_n, the incremental numerical damping work is computed as:

$$\Delta W_k(t_n) = \alpha \, \Delta t \sum_{b \in \mathcal{B}} \left(|F^{(b)}_{u,x}| \, |v^{(b)}_x| + |F^{(b)}_{u,y}| \, |v^{(b)}_y| + |F^{(b)}_{u,z}| \, |v^{(b)}_z| \right), \tag{56}$$

where α is the local damping coefficient (Eq. 9), Δt is the mechanical timestep, $\boldsymbol{F}^{(b)}_u = (F^{(b)}_{u,x}, F^{(b)}_{u,y}, F^{(b)}_{u,z})$ is the unbalanced force of block b, $\boldsymbol{v}^{(b)} = (v^{(b)}_x, v^{(b)}_y, v^{(b)}_z)$ is the block translational velocity, and $\mathcal{B}$ denotes the set of blocks excluding boundary blocks.
The cumulative numerical damping work is then obtained as:

$$W_k(t_N) = \sum_{n=1}^{N} \Delta W_k(t_n). \tag{57}$$

Fig. 19 compares the cumulative physical dissipation E_{phys} and the cumulative work removed by local numerical damping W_k, evaluated at cycle-peak drift levels in negative and positive loading directions for

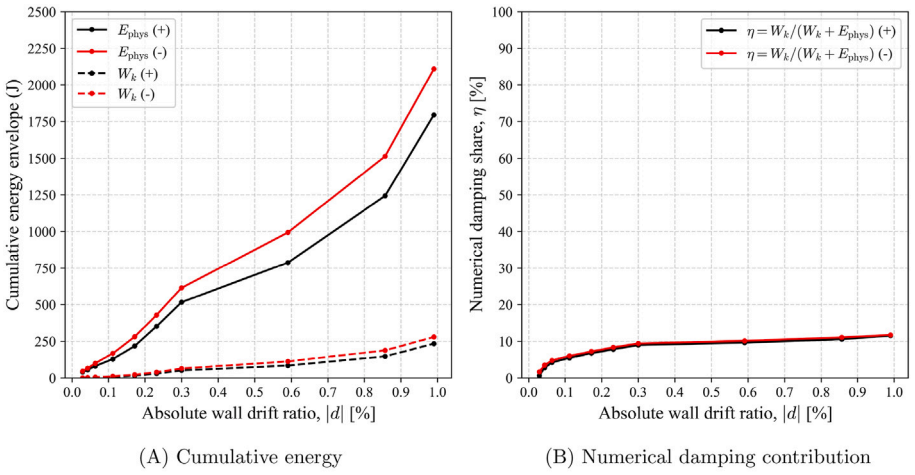

(A) Cumulative energy (B) Numerical damping contribution

Fig. 19. Energy-based assessment of numerical damping for the benchmark case of TUD-COMP-0a.

the benchmark case TUD-COMP-0a. It is important to note that the local damping coefficient α is set to 0.8 by default. Fig. 19(A) shows the corresponding energy envelopes for both loading directions, while Fig. 19(B) reports the numerical damping share:

$$\eta = \frac{W_k}{W_k + E_{\text{phys}}} \tag{58}$$

The energy envelopes reveal a clear separation in magnitude between physical and numerical contributions over the entire drift range. Physical dissipation increases rapidly with imposed deformation, reflecting progressive cracking, sliding, and compressive damage at the joint level. In contrast, the numerical damping grows gradually and remains substantially smaller. At the largest drift levels of 1.0 %, E_{phys} reaches more than 2000 J, whereas W_k remains on the order of 250 J for both loading directions.

The evolution of the damping share η further confirms this observation. After an initial increase at small drift levels, where both physical dissipation and damping are limited, the ratio stabilizes with increasing deformation and remains below approximately 10 % to 12 % throughout the analysis. Importantly, no late-stage increase of η is observed, even at large drift levels approaching mechanism formation. This indicates that numerical damping does not progressively dominate the response as damage accumulates.

The close agreement between positive and negative loading cycles also demonstrates that the numerical damping contribution is symmetric and does not introduce spurious directional bias into the cyclic response. Overall, the results show that local numerical damping remains a secondary, non-governing component of the total energy dissipation in the benchmark case considered. The global response is therefore controlled by constitutive dissipation mechanisms embedded in the joint model rather than by algorithmic energy removal. It is acknowledged, however, that the relative contribution of numerical damping may be problem-dependent and influenced by factors such as geometry, loading protocol, and choices of constitutive parameters. A systematic investigation of the sensitivity of numerical dissipation to these aspects will be conducted in future work.

5.2. Failure mechanism transition in in-plane loading cases

This section analyses the evolution of the failure mechanism in specimen TUD-COMP-0a, tested under double-clamped boundary conditions, as it transitions from flexure-dominated rocking to friction-controlled sliding [65], with an emphasis on the attendant stress redistribution and damage localization. Although specimen TUD-COMP-1 also displayed a hybrid rocking–sliding response, the discussion below is confined to TUD-COMP-0a to isolate the effects of double clamping and enable a focused examination of the governing mechanics.

Fig. 20(A) captures the evolving failure mechanism of specimen TUD-COMP-0a by plotting the normal and shear stress paths at the compressed toes at the bottom-right corner of the wall. Stress paths shown are taken at the compressed toe. Along these histories, the shear surface F_2 is not violated. The only surface reached during cyclic loading is the tensile cut-off F_1, which is not visible here due to the much smaller tensile scale compared with the compressive stresses at the toe. During the 4th and 7th loading cycles (represented by cycle number 6 in Fig. 20(B), the normal-shear stress trajectories for both toes stay well inside the yield surface, forming small closed loops produced by repeated loading–unloading while one toe is compressed and the opposite toe lifts off. Since the stress state never reaches the envelope at this stage, the shear transfer is negligible, and the response is governed by pure rocking, where the wall returns to the original hinge point at both toes.

Between the 8th and 10th loading cycles (represented by cycle number 8 in Fig. 20(B), stepwise cracks formed in the pier, raising the shear demand at the compressed toes. The stress paths shift upward toward the compression cap while the normal compressive stress approaches 3.5 MPa to 4 MPa. However, at this state, the sliding mechanism is still inactive, as evident by the unloading trajectories that return to the origin. This behavior is also consistent with the global response in Fig. 15(A) and 16(A), where a slight dissipated energy is observed between cycles 8 and 10.

In the final loading cycles (cycle 11 in Fig. 20(B), the averaged normal-shear stress state at the joint plane approaches the compression cap and, during unloading, intersects the Coulomb friction line. Notably, the plotted stress states are averaged over the contact points forming the joint at the bottom-right corner. As a result, yielding in Fig. 20(A) and Fig. 20(B) occurs before the average stress state visibly reaches the compression cap line. At this stage, the entire length of the bed-joint segment along the compressed toe yields in shear, enabling slip to propagate continuously along the interface. Simultaneously, local crushing initiates at the compressed toe. Consequently, the rocking mechanism becomes secondary to friction-controlled sliding, shifting the hinge location and resulting in the residual drift observed in Fig. 15(A). Fig. 21 shows the sequential deformed shape (magnified 30 times) of specimen TUD-COMP-0a as wall drift, δ, increases from 0 % to 1 % at the last loading cycle. For drifts up to about 0.5 %, the pier behaves almost as a rigid body, rocking about one toe while the opposite toe lifts off, and relative slip along the bed-joint remains negligible.

Once δ exceeds this threshold, the pier begins to translate with respect to the loading toes, and by 0.8 % to 1.0 % drift, the response is sliding-dominated: the entire bed-joint has yielded in shear, local

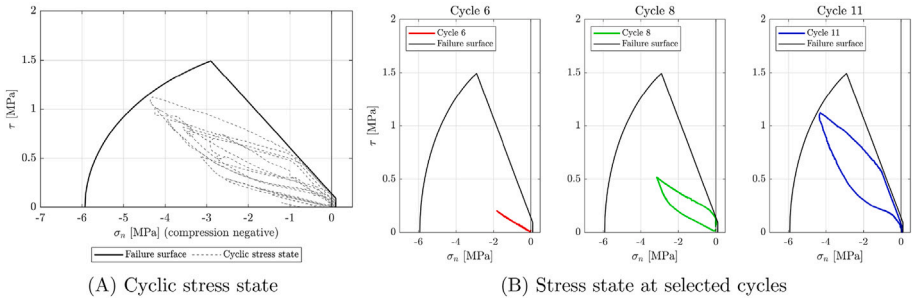

Fig. 20. The shear vs normal stresses evolution of TUD-COMP-0a model at the compressed toe (bottom-right corner).

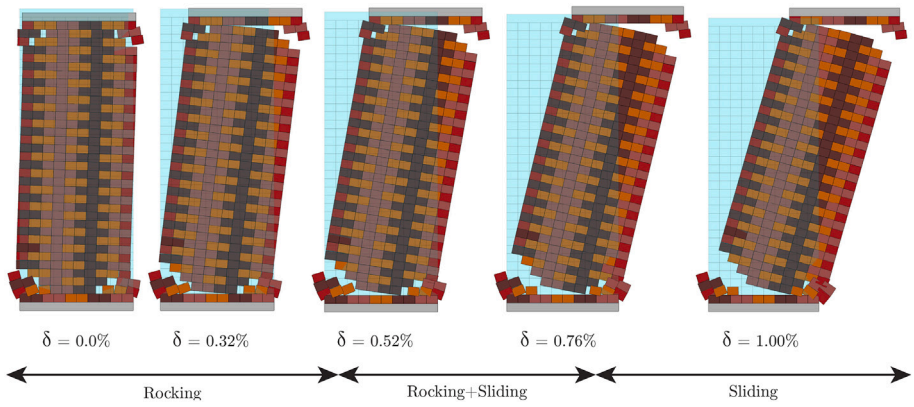

Fig. 21. Deformed shapes of TUD-COMP-0a at the last positive loading cycle from 0 % to 1 % drift (Magnified 30x).

crushing appears at the compressed toe, and rocking plays only a secondary role. This demonstrates that the multi-surface failure surface used in the proposed modelling strategy can reproduce the drift-dependent transition from the rocking mechanism at lower drift to the sliding mechanism at higher drift.

5.3. Sensitivity analysis of the imposed displacement rate on the loading scheme

To assess the influence of the imposed displacement rate on the global response and to verify the quasi-static validity of the constitutive model, a velocity sensitivity study was conducted on specimen TUD-COMP-0a. Five peak loading velocities were considered: v = 0.5, 1.0, 2.5, 5.0, and 10.0 mm/s, while boundary conditions, material properties, and the cyclic protocol were kept unchanged. Because the imposed motion follows the cosine–plateau–cosine history defined in Eqs. (44) and (45), variations in $v_{\max}$ directly modify the ramp durations (t_a, t_b) and, consequently, the total actuation time (t_{tot}). Thus, higher loading velocities result in proportionally shorter actuation times to reach the same prescribed displacement.

The imposed velocities are numerical drivers for dynamic relaxation, not experimental actuation rates. The quasi-static solutions are sought by using sufficiently small kinetic energy ratios and residual force tolerances during the analyses. Within these checks, lowering the velocity down to $0.5\,\mathrm{mm\,s^{-1}}$ affects peak and envelope stiffness only marginally but increases the runtime markedly, whereas higher velocities risk spurious inertial effects. The value $10\,\mathrm{mm\,s^{-1}}$ is used only as an upper-bound driver to limit runtime, not as a physical rate.

Fig. 22 compares the force–drift hysteresis at different velocities against the experimental benchmark, while Fig. 23 shows the corresponding dissipated energy per cycle. In general, the sensitivity study confirms that the global response is only weakly dependent on the imposed velocity in the quasi-static range: peak strengths remain nearly unchanged, drift levels at maximum force are consistent, and the main differences arise in the shape of the hysteresis loops and the magnitude of dissipated energy. These observations suggest the residual discrepancies arise from velocity-dependent artifacts of the explicit solver.

At the lowest velocities (0.5 [mm/s] to 1.0 [mm/s]), the loops are somewhat more pinched, but the dissipated energy at $0.5\,\mathrm{mm\,s^{-1}}$ agrees closely with the experimental trend, particularly in the largest cycles. At intermediate velocities ($2.5\,\mathrm{mm\,s^{-1}}$ to $5.0\,\mathrm{mm\,s^{-1}}$), the global hysteresis is reproduced well, though the energy per cycle is slightly underestimated at peak drift levels. At the highest velocity ($10.0\,\mathrm{mm\,s^{-1}}$), the loops widen and energy dissipation is artificially amplified due to dynamic effects, which are not captured by the quasi-static constitutive laws. The cycle-by-cycle energy results in Fig. 23 confirm that the $2.5\,\mathrm{mm\,s^{-1}}$ to $5.0\,\mathrm{mm\,s^{-1}}$ case provides the closest match to the experimental dissipation, while higher velocities either underestimate or prematurely amplify the energy. Nevertheless, the intermediate range ($2.5\,\mathrm{mm\,s^{-1}}$ to $5.0\,\mathrm{mm\,s^{-1}}$) still offers a good compromise, reproducing the overall growth pattern of dissipated energy while maintaining feasible computational times.

The quantitative results are summarized in Table 4. Across all velocities, simulated peak loads deviate only by about 3 % to 4 % in the positive direction and 6 % to 7 % in the negative direction from the experimental reference, confirming the robustness of the model predictions. Using the same computational resource (3.5 GHz Intel Xeon CPU with four cores and 32 GB of memory), computational time varies by more than an order of magnitude, ranging from about 185 h at 0.5 mm/s to 10 h at 10 mm/s, underscoring the trade-off between accuracy and efficiency.

Based on these observations, velocities in the intermediate range of $2.5\,\mathrm{mm\,s^{-1}}$ to $5.0\,\mathrm{mm\,s^{-1}}$ are recommended as a practical compromise: they reproduce the global hysteresis with reasonable fidelity, capture the cycle-by-cycle energy evolution reasonably well, and keep

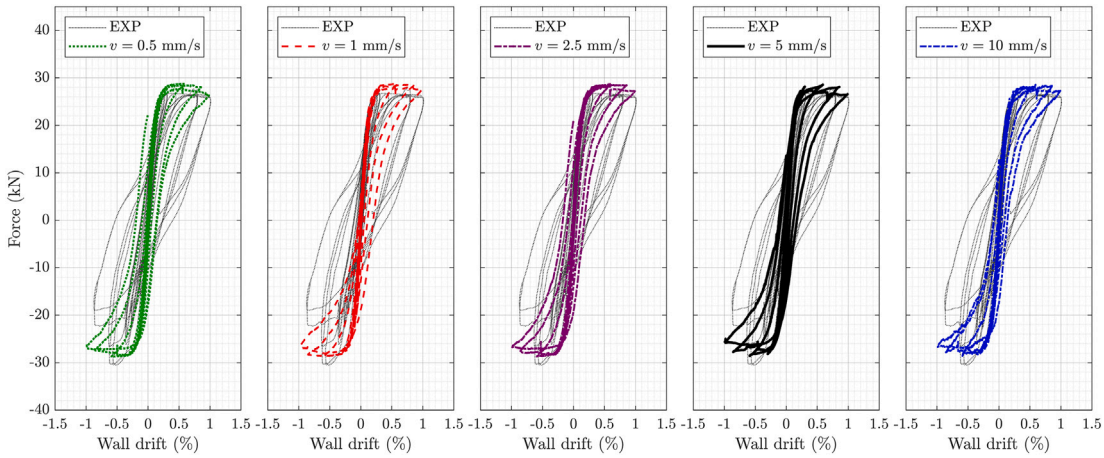

Fig. 22. Force–drift hysteresis of specimen TUD-COMP-0a under different loading velocities compared with experimental results.

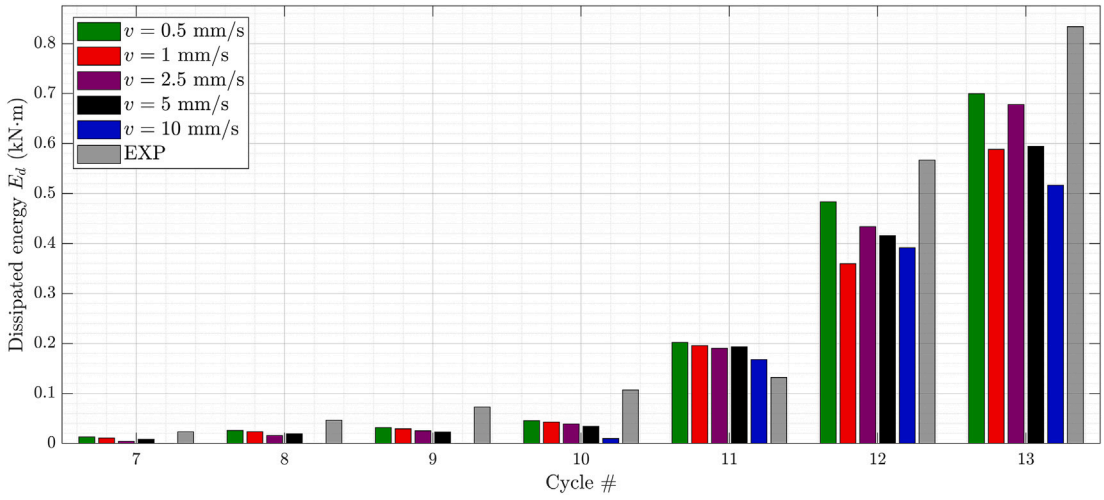

Fig. 23. Cycle-by-cycle dissipated energy of specimen TUD-COMP-0a under different loading velocities compared with experimental results.

Table 4
Velocity sensitivity results for specimen TUD-COMP-0a.

v [mm/s]	F_{pos} [kN]	F_{neg} [kN]	$Drift_{pos}$ [%]	$Drift_{neg}$ [%]	Time [h]
0.5	28.74 (3.8 %)	−28.70 (6.1 %)	0.590 (–19.7 %)	−0.591 (–13.5 %)	185
1.0	28.76 (3.9 %)	−28.64 (6.3 %)	0.591 (–19.7 %)	−0.590 (–13.5 %)	86
2.5	28.71 (3.7 %)	−28.69 (6.2 %)	0.591 (–19.7 %)	−0.590 (–13.5 %)	32
5.0	28.60 (3.3 %)	−28.57 (6.6 %)	0.590 (–19.7 %)	−0.591 (–13.5 %)	26
10.0	28.60 (3.3 %)	−28.57 (6.6 %)	0.591 (–19.7 %)	−0.590 (–13.5 %)	10

EXP values: $F_{pos,EXP} = 27.69$ kN, $F_{neg,EXP} = -30.58$ kN, $\delta_{pos,EXP} = 0.736\%$, $\delta_{neg,EXP} = -0.520\%$.

computational demands within manageable limits. Nevertheless, this recommendation should be regarded as case-specific. The optimal loading rate may vary depending on specimen geometry, boundary conditions, and material properties, and thus requires verification for each application.

All simulations in this study are performed in a quasi-static (dynamic-relaxation) setting: slow loading with local numerical damping. This choice isolates the constitutive/interface behavior and leverages the explicit scheme's robustness in the presence of softening and contact evolution. The extension to fully dynamic analyses is conceptually straightforward within the same framework (use physical time histories, minimize or remove numerical local damping, and include appropriate rate effects), but lies beyond the scope of the present work and is reserved for future work.

5.4. Comparison to other numerical methods

In this section, the proposed modelling strategy is evaluated against numerical approaches from the literature that validated the same experimental tests. For the double-clamped and squat specimen TUD-COMP-4, the comparison is made with the study of Sousamli [66], which used the Plasticity-based Combined Cracking, Crushing, and Shearing (PCCCS) interface model of Lourenço and Rots [19]. For the cantilever-squat specimen TUD-COMP-6, the reference is the Damaging Block-based (D-BB) model by D'Altri et al. [9], where blocks interact through damaging interfaces. The PCCCS model was implemented in DIANA FEA (v10.4) and the D-BB model as a user-defined law in Abaqus/Standard, both employing implicit solvers. The results of these models were taken directly from the respective publications [9,66]; the present authors did not reproduce them.

Table 5
Material properties for the cross-validation of the proposed modelling strategy.

Properties	Symbol	Unit	TSC[1]		PCCCS		D-BB
			Head joint	Bed joint	Head joint	Bed joint	–
Normal stiffness	k^n	GPa m^{-1}	52.17	52.17	10.44	121.2	75
Shear stiffness	k^s	GPa m^{-1}	22.49	22.49	16.36	39.31	7.5
Tensile strength	f_t	MPa	0.003	0.105	0.003	0.105	0.12
Cohesion	c	MPa	0.014	0.14	0.14	0.14	0.11
Friction coefficient	μ	[-]	0.466	0.466	0.43	0.43	0.55
Mode-I fracture energy	G_I	N m^{-1}	8.38	8.38	0.007	7.75	–
Mode-II fracture energy	G_{II}	N m^{-1}	83.8	83.8	100	3000	–
Compressive strength	f_c	MPa	5.93	7.0	7.55	5.93	–
Compressive fracture energy	G_c	N m^{-1}	15,000	31,500	34,000	15,000	–
Additional parameters							
Ultimate separation	u_k	m	–	–	–	–	0.001
Ultimate slip	δ_k	m	–	–	–	–	0.001
Tension brittleness	ζ	[-]	–	–	–	–	8.0
Shear brittleness	ξ	[-]	–	–	–	–	4.0
Cap shear parameter	C_s	[-]	12		5		–
Brick unit properties							
Young's modulus	E_b	MPa	–	–	8990		4800
Poisson's ratio	υ	[-]	–	–	0.14		0.14
Compressive strength	f_{c_b}	MPa	–	–	–	–	6.8
Tensile strength	f_{t_b}	MPa	1.0	1.0	–	–	1.5

[1] Same material properties are applied to TUD-COMP-0a and TUD-COMP-1.

Since no validated experimental data currently exist for the slender specimens of TUD-COMP-0a and TUD-COMP-1, the comparative assessment is performed through numerical simulations conducted by the authors in *3DEC* using the joint constitutive model proposed by Pulatsu [8]. This joint model, referred to as the Tension-Shear–Compression (TSC) joint model, is based on a multi-surface damaged plasticity formulation, where failure in the compressive regime is governed by a compression cut-off mechanism [34]. This approach contrasts with the compression cap yield surface adopted in the present study, which allows for more gradual confinement-dependent yielding under compression.

Moreover, the TSC model incorporates linear softening behavior across tensile, shear, and compressive failure regimes, in contrast to the damage progression laws employed in the current study. These differences in constitutive modelling are expected to influence the stress redistribution and failure mechanisms observed in the numerical results, and must be considered when interpreting the comparative outcomes between the two approaches.

The parameters used in the corresponding models for cross-comparison are summarized in Table 5. The properties are categorized according to different constitutive models used in the cross-comparison, with specific differentiation between head joints and bed joints whenever possible. The TSC model uses the identical material properties described in Table 3, except for the peak ratio n, as the TSC model employs a linear softening law for the compressive behavior. Meanwhile, the D-BB model [9] requires additional interface characteristics in tension and shear to describe the post-peak softening and damage evolution. In contrast, the PCCCS model [19,66] uses the fracture energy terms to address the post-peak softening in tension, shear, and compression regimes. The brick unit properties are given in Table 5, as the PCCCS and D-BB models use deformable block configurations, while the TSC model uses a potential crack plane at the brick's mid-length to address the unit-splitting failure. Furthermore, the units in the D-BB model follow the continuum plastic-damage constitutive law to address the compressive and tensile failure of the brick units.

Figs. 24(A) and 24B present the force–drift responses of specimens TUD-COMP-0a and TUD-COMP-1, respectively, simulated using the Tension-Shear–Compression (TSC) joint model proposed by Pulatsu [8]. Overall, the simulated responses exhibit reasonable agreement with the experimental observations, particularly in the initial linear range.

However, some deviations become evident in the nonlinear regime, particularly beyond a drift level of approximately 0.1 %. While the TSC model captures the initial stiffness and peak strength with reasonable accuracy, it tends to underpredict the energy dissipation observed during the later loading cycles. This behavior can be attributed to the model's simplified representation of stiffness degradation and its use of linear softening laws.

In the case of TUD-COMP-0a (Fig. 24(A), the TSC model predicted a slightly higher peak load of approximately 30 kN, compared to 28 kN obtained using the proposed modelling strategy. Additionally, the TSC model exhibited limited energy dissipation, with minimal hysteretic behavior observed from one cycle to the next. The loops were only evident during the final loading cycle, where noticeable residual drift indicated some inelastic behavior.

A similar trend was observed for TUD-COMP-1 (Fig. 24(B). Both the TSC model and the proposed modelling strategy predicted a comparable peak load of approximately 12.5 kN, indicating consistent performance in capturing the specimen's strength capacity. However, in terms of cyclic behavior, the TSC model again showed limited hysteretic response and underrepresented the extent of energy dissipation throughout the loading cycles. Unlike in TUD-COMP-0a, where some inelastic behavior emerged in the final cycle, the TSC model did not exhibit noticeable hysteresis at any stage of the loading for TUD-COMP-1.

The differences in hysteretic behavior between the two models can be primarily attributed to the formulation of the failure surface in the shear–compression domain. The proposed model utilizes a compression cap yield surface that evolves with increasing axial stress, enabling a more gradual and distributed shear failure. This effectively captures the inelastic deformation and energy dissipation observed in experiments. In contrast, the TSC model uses a compression cut-off, which imposes a more abrupt limit on compressive failure and reduces the interaction between axial and shear behavior. While this simplification may improve computational efficiency, it can delay the onset of shear failure and limit the model's ability to reproduce progressive damage mechanisms. As a result, even with identical masonry compressive strengths, the model

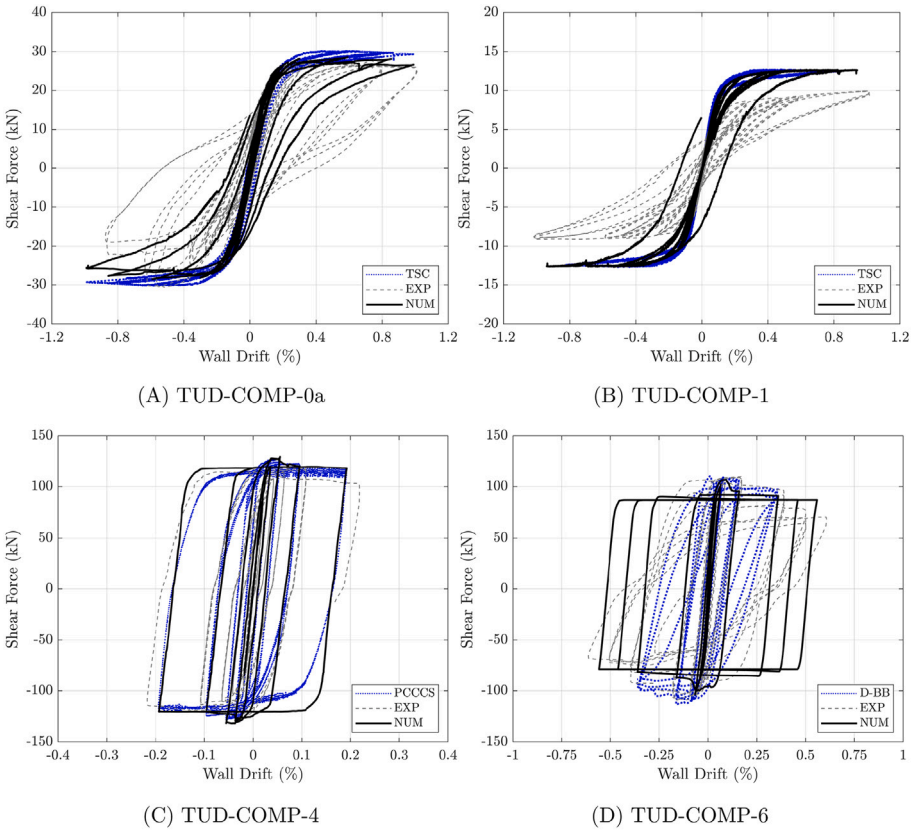

Fig. 24. Cross-comparison of validated wall specimens.

with a compression cap tends to initiate shear failure earlier than the one with a compression cut-off. This difference is particularly relevant in the case of hybrid rocking-shear failure, when a transition from the former to the latter mechanism is expected, since the shear sliding occurs in the highly compressed toes.

Fig. 24(C) and Fig. 24(D) show the force–drift response of the TUD-COMP-4 and TUD-COMP-6 specimens, respectively, comparing the numerical prediction from the proposed model (NUM) and the respective reference simulations (PCCCS [19,66] for TUD-COMP-4 and D-BB [9] for TUD-COMP-6) to the experimental results (EXP). It can be observed that the proposed strategy aligns generally with other modelling strategies presented in the literature.

For TUD-COMP-4 (Fig. 24(C)), the proposed model shows close agreement with both the experimental results (EXP) and the reference PCCCS simulation. Taking advantage of the larger time step afforded by the implicit solution scheme and the stable pre-peak response, the loading sequence was repeated three times per cycle to ensure consistent hysteretic behavior. Compared to the PCCCS model, the proposed approach yields slightly larger hysteresis loops in the final loading cycle; however, both responses remain well within the experimental envelope. The accurate reproduction of the peak load values and the characteristic pinching across cycles underscores the model's enhanced ability to capture joint opening, interface friction, and softening mechanisms. It is worth noting that while Sousamli [6] reported the PCCCS model to be effective in reproducing shear-dominated responses such as in TUD-COMP-4, its accuracy was reduced for specimens governed by hybrid rocking–shear mechanisms.

In the case of TUD-COMP-6 (Fig. 24(D)), the proposed modelling approach shows relatively good agreement with both the experimental data and the D-BB reference model up to the same drift level of 0.27 %. Beyond this point, the D-BB model exhibits divergence of the incremental-iterative procedure, primarily due to excessive localized damage at the compressed toe regions of the wall [9]. In contrast, while the proposed model displays slightly larger hysteresis loops and a more gradual reduction in shear capacity compared to the experiment, it remains stable and capable of completing the full loading sequence, consistent with the experimental procedure. This highlights the robustness and reliability of the proposed modelling strategy in capturing both cyclic behavior and progressive damage across various masonry wall configurations.

Direct runtime comparisons with external FEM/DEM studies were not performed in this paper because publicly available results typically report only response curves and failure mechanisms. Even where runtimes are given, they are tied to different hardware, meshing/preprocessing pipelines, solver tolerances, and contact regularizations, precluding an apples-to-apples assessment. The efficiency claims in this paper are therefore qualitative, grounded in the absence of nonlinear iterations and in the robustness of the explicit time-marching scheme through softening and contact evolution. Quantitative timings are meaningful primarily within a controlled environment, which lies outside the scope of this paper.

6. Conclusions

This study presented a comprehensive cyclic joint constitutive model for unreinforced masonry (URM) structures, developed within the Distinct Element Method (DEM) framework. The model addresses a key challenge in simulating the nonlinear and hysteretic behavior of masonry interfaces subjected to cyclic loading. It incorporates a unified yield surface, combining tensile cut-off, Coulomb friction, and a

compression cap, alongside exponential softening in tension and shear, a hardening–softening law in compression, and a nonlinear unloading–reloading mechanism to simulate energy dissipation. To capture dilatant effects more realistically, a novel uplift correction mechanism was introduced, coupled with an exponential decay law for dilatancy softening. The proposed model was implemented in *3DEC*, a commercial DEM platform, leveraging an explicit time-marching integration scheme for robust and stable simulations under large displacements. The model was rigorously validated at both material and structural levels. The main findings of the validations and subsequent discussions can be summarized as follows:

- At the material-level, numerical simulations of cyclic uniaxial compression and direct shear tests reproduced key experimental features with great accuracy, including energy dissipation and stiffness degradation under cyclic loading. The results confirmed the model's ability to reproduce fundamental constitutive behaviors of masonry interfaces under isolated conditions.
- Validation of the triplet test demonstrated that the novel dilatancy uplift correction, combined with an exponential decay law for the dilatancy angle, realistically captured the progressive reduction of joint opening under shear.
- At the structural level, validation on four full-scale calcium silicate masonry walls under combined compression and cyclic in-plane loading (with varying boundary conditions and aspect ratios) showed that the model successfully reproduced the global hysteretic response, including force–drift loops and cycle-by-cycle energy dissipation, as well as local failure mechanisms such as joint cracking, sliding, diagonal shear cracking, and toe crushing.
- An energy-based assessment performed on the benchmark case TUD-COMP-0a, with double-clamped and slender configuration, shows that the contribution of local numerical damping remains secondary and non-governing with respect to the physical dissipation captured by the joint constitutive model, with no evidence of directional bias under cyclic loading.
- The modelling strategy accurately simulated the drift-dependent transition in slender wall specimens from initial rocking-dominated behavior at low drift to friction-controlled sliding at higher drift levels, aligning with observed experimental trends.
- The velocity sensitivity study confirmed that, although the model operates in a quasi-static regime, the imposed displacement rate exerts only a modest influence on hysteretic behavior and energy dissipation once nonlinear mechanisms become active. Very low velocities (e.g., 0.5 mm/s) provide the closest agreement with experimental energy dissipation, while intermediate velocities (2.5–5 mm/s) offer a balance between accuracy and computational efficiency. The optimal choice of velocity remains case-dependent and should be verified for each application.
- Comparative analyses were conducted against three established approaches: the Plasticity-based Combined Cracking Crushing Shearing (PCCCS) model in DIANA for the squat double-clamped specimen, the Damaging Block-Based (D-BB) model in Abaqus/Standard for the squat cantilever specimen, and a DEM-based Tension, Shear, Crushing (TSC) interface model for the slender specimens. The proposed model performed on par with these reference methods in terms of force–displacement response. Unlike implicit solvers, however, the proposed model exhibited no convergence issues, even under conditions of large displacement or nonlinear response.

Overall, the proposed cyclic constitutive model provides an efficient framework for simulating the seismic behavior of masonry structures within the DEM framework. Its ability to capture complex material and structural responses, validated against experiments and benchmarked with alternative modelling strategies, demonstrates its value as a practical tool for performance assessment, retrofit design, and the conservation of historical URM systems under cyclic and seismic loading. A comprehensive sensitivity/identification study of the empirical/default parameters is valuable, but beyond the scope of this paper. Here, the initial slope in k_n and k_s is intentionally tuned to the experimental test, and a targeted adjustment is made to Eq. (30) to account for the small-displacement compliance of the rigid block formulation and the different behavior pre- and post-peak under uniaxial compression. All other parameters are set from tests or literature and kept fixed, so peak strength, post-peak softening, and failure mechanisms are predictive outcomes rather than calibration targets. Future work on this paper will address the sensitivity of the empirical parameters included in the formulation.

This rigid-block interface formulation is applicable to both in-plane and out-of-plane actions. In this study, the focus is on in-plane loading and validation; however, this does not limit its applicability to out-of-plane scenarios. Future developments will focus on extending the model to address out-of-plane (OOP) response and on validating full-scale URM buildings and retrofitted systems. The problem dependence of the energy-based assessment will also be investigated in various masonry typologies. In addition, the model will be applied to real-world case studies on vulnerability assessment and performance-based engineering of historical masonry assets. Finally, although this study focuses on in-plane quasi-static response using dynamic relaxation, the formulation extends to genuinely dynamic analyses by prescribing physical time histories, minimizing numerical damping, and including rate/impact effects as needed. A dedicated dynamic validation will be pursued in future work.

CRediT authorship contribution statement

Yopi P. Oktiovan: Writing – original draft, Visualization, Validation, Software, Methodology, Formal analysis, Conceptualization. **Francesco Messali:** Writing – review & editing, Supervision, Project administration, Methodology, Data curation, Conceptualization. **Bora Pulatsu:** Writing – review & editing, Supervision, Resources, Conceptualization. **Satyadhrik Sharma:** Writing – review & editing, Visualization, Validation, Methodology, Data curation. **José V. Lemos:** Writing – review & editing, Software, Methodology, Conceptualization. **Jan G. Rots:** Writing – review & editing, Project administration, Methodology, Funding acquisition, Conceptualization.

Declaration of competing interest

The authors declare that they have no known competing financial interests or personal relationships that could have appeared to influence the work reported in this paper.

Acknowledgements

The authors would like to acknowledge the support of Itasca Inc. through the Itasca Educational Partnership (IEP) Teaching Program. The authors also gratefully acknowledge Dr. Nicolò Damiani for his valuable input in developing the velocity profile used in the cyclic loading simulations. The authors would also like to thank Prof. Francesco Graziotti for providing the triplet test data used for material-level validation.

Appendix A. Normal force evaluation in a nonlinear interface

Require: u_n, Δu_n, F_n, ΔF_n, material & history vars
Ensure: Updated F_n, ΔF_n

if $u_n < 0$ **then**
  if $u_n + \Delta u_n \geq u_{n,\text{hist,ten}}$ **then**
    $u_{n,\text{hist,ten}} \leftarrow u_n$
  end if
  Compute F_n from Eq. (12)
  return
else
  if $u_n + \Delta u_n \leq u_{n,\text{hist,comp}}$ **and** reloadFlag $= 0$ **then**
    $u_{n,\text{hist,comp}} \leftarrow -u_n$
  end if
  if $\sigma_n + \Delta\sigma_n \geq \sigma_{\text{hist,comp}}$ **then**
    if $u_n + \Delta u_n \leq u_{\text{el,limit}}$ **then**
      Compute F_n from Eq. (12)
    else if $\sigma_n + \Delta\sigma_n \leq f_c$ **then**
      Compute σ_n from Eq. (22)
      $F_n \leftarrow \sigma_n A_c$
      PlasticFlag $= 1.0$
    end if
    return
  else
    Calculate $u_{n_{pl}}$ from Eq. (30)
    if $\Delta u_n \geq 0$ and PlasticFlag $= 1.0$ **then**
      if $u_n + \Delta u_n \geq u_{\text{hist,comp}} \cdot 0.985$ **then** ▷ perturbation Check for instabilities
        Compute F_n from Eq. (12)
      else
        Compute σ_n from Eq. (31)
        $F_n \leftarrow \sigma_n A_c$
        Record $f_{m_{ro}}$ and $u_{n_{ro}}$ for reloading purpose
        reloadFlag $= 1.0$
      end if
      return
    else if reloadFlag $= 1.0$ **and** $\Delta u_n \leq 0$ **then**
      $\beta \leftarrow$ recovery factor (Eq. (37)
      $k_r \leftarrow \frac{\beta f_{\text{peak}} - f_{m,\text{ro}}}{u_{n,\text{hist,comp}} - u_{n,\text{ro}}}$
      Calculate σ_n from Eq. (35)
      $\sigma_{\text{env}} \leftarrow$ Eq. (22) or Eq. (23)
      if $\sigma_n < \sigma_{\text{env}}$ **then**
        $F_n \leftarrow \sigma_n A_c$
      else
        reloadFlag $\leftarrow 0$
        $F_n \leftarrow \sigma_{\text{env}} A_c$
      end if
    end if
  end if
end if

Appendix B. Joint compression damage scalar for TUD-COMP-0a and TUD-COMP-6

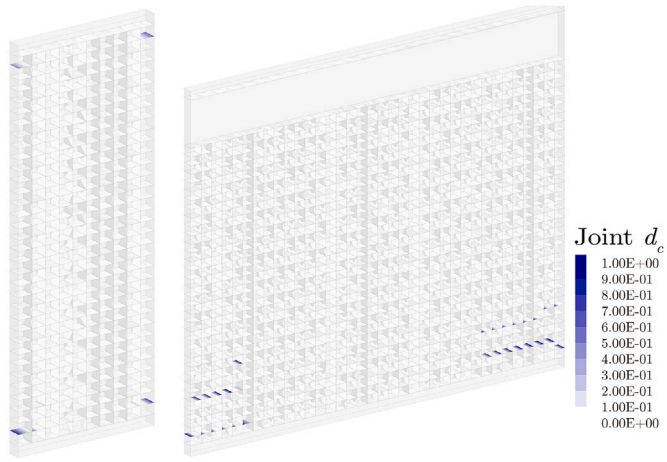

(A) TUD-COMP-0a (B) TUD-COMP-6

Fig. B.25. Joint compression damage scalar plot at the end of analysis.

Data availability

The data that support the findings of this study are available from the corresponding author upon reasonable request.

References

[1] Lourenco PB. Computational strategies for masonry structures [Ph.D. thesis]. Delft, Netherlands: Delft University of Technology; 1996.
[2] Lagomarsino S, Penna A, Galasco A, Cattari S. TREMURI program: an equivalent frame model for the nonlinear seismic analysis of masonry buildings. Eng Struct 2013;56:1787–99. https://doi.org/10.1016/J.ENGSTRUCT.2013.08.002
[3] Camata G, Marano C, Sepe V, Spacone E, Siano R, Petracca M, Roca P, Pelà L, et al. Validation of non-linear equivalent-frame models for irregular masonry walls. Eng Struct 2022;253:113755. https://doi.org/10.1016/J.ENGSTRUCT.2021.113755
[4] Calderini C, Lagomarsino S. A micromechanical inelastic model for historical masonry. J Earthq Eng 2006;10(4):453–79. https://doi.org/10.1080/13632460609350605
[5] Berto L, Saetta A, Scotta R, Vitaliani R. An orthotropic damage model for masonry structures. Int J Numer Methods Eng 2002;55(2):127–57. https://doi.org/10.1002/NME.495
[6] Sousamli M, Messali F, Rots JG. A total-strain based orthotropic continuum model for the cyclic nonlinear behavior of unreinforced brick masonry structures. Int J Numer Methods Eng 2022;123(8):1813–40. https://doi.org/10.1002/NME.6917
[7] Nodargi NA, Bisegna P. A mixed finite element for the nonlinear analysis of in-plane loaded masonry walls. Int J Numer Methods Eng 2019;120(11):1227–48. https://doi.org/10.1002/NME.6179
[8] Pulatsu B. Coupled elasto-softening contact models in DEM to predict the in-plane response of masonry walls. Comput Part Mech 2023;10:1759–70. https://doi.org/10.1007/s40571-023-00586-x
[9] D'Altri AM, Messali F, Rots J, Castellazzi G, de Miranda S. A damaging block-based model for the analysis of the cyclic behaviour of full-scale masonry structures. Eng Fract Mech 2019;209:423–48. https://doi.org/10.1016/j.engfracmech.2018.11.046
[10] Minga E, Macorini L, Izzuddin BA. A 3d mesoscale damage-plasticity approach for masonry structures under cyclic loading. Meccanica 2018;53(7):1591–611. https://doi.org/10.1007/S11012-017-0793-Z/FIGURES/25

[11] Macorini L, Izzuddin BA. A non-linear interface element for 3d mesoscale analysis of brick-masonry structures. Int J Numer Methods Eng 2011;85(12):1584–608. https://doi.org/10.1002/nme.3046

[12] Oktiovan YP, Messali F, Pulatsu B, Lemos JV, Rots JG. A contact-based constitutive model for the numerical analysis of masonry structures using the distinct element method. Comput Struct 2024;303:107499. https://doi.org/10.1016/J.COMPSTRUC.2024.107499

[13] Andreotti G, Graziotti F, Magenes G. Detailed micro-modelling of the direct shear tests of brick masonry specimens: the role of dilatancy. Eng Struct 2018;168:929–49. https://doi.org/10.1016/J.ENGSTRUCT.2018.05.019

[14] Lemos JV, Sarhosis V. Discrete element bonded-block models for detailed analysis of masonry. Infrastructures 2022;7(3):31. https://doi.org/10.3390/infrastructures7030031

[15] D'Altri AM, de Miranda S, Castellazzi G, Sarhosis V. A 3d detailed micro-model for the in-plane and out-of-plane numerical analysis of masonry panels. Comput Struct 2018;206:18–30. https://doi.org/10.1016/J.COMPSTRUC.2018.06.007

[16] Nie Y, Sheikh A, Visintin P, Griffith M. A robust computational strategy for failure prediction of masonry structures using an improved multi-surface damage-plastic based interface model. Int J Numer Methods Eng 2023;124(11):2498–528. https://doi.org/10.1002/NME.7218

[17] Lotfi HR, Shing PB. Interface model applied to fracture of masonry structures. J Struct Eng 1994;120(1):63–80. https://doi.org/10.1061/(ASCE)0733-9445(1994)120:1(63)

[18] Xie Z, Sousamli M, Messali F, Rots JG. A sub-stepping iterative constitutive model for cyclic cracking-crushing-shearing in masonry interface elements. Comput Struct 2021;257:106654. https://doi.org/10.1016/J.COMPSTRUC.2021.106654

[19] Lourenço PB, Rots JG. Multisurface interface model for analysis of masonry structures. J Eng Mech 1997;123(7):660–8. https://doi.org/10.1061/(ASCE)0733-9399(1997)123:7(660)

[20] Simo JC, Hughes TJR editor. Computational inelasticity. 1 ed. vol. 1. Springer Science & Business Media; 1998. https://doi.org/10.1007/B98904

[21] Ortiz M, Popov EP. Accuracy and stability of integration algorithms for elastoplastic constitutive relations. Int J Numer Methods Eng 1985;21(9):1561–76. https://doi.org/10.1002/nme.1620210902

[22] Wilkins ML. Calculation of elastic-plastic flow. New York: University of California, Berkeley Academic Press; 1963. p. 66 [Chap. 6].

[23] Pérez-Foguet A, Armero F. On the formulation of closest-point projection algorithms in elastoplasticity—part II: globally convergent schemes. Int J Numer Methods Eng 2002;53(2):331–74. https://doi.org/10.1002/NME.279

[24] Sloan SW. Substepping schemes for the numerical integration of elastoplastic stress–strain relations. Int J Numer Methods Eng 1987;24(5):893–911. https://doi.org/10.1002/NME.1620240505

[25] Aref AJ, Dolatshahi KM. A three-dimensional cyclic meso-scale numerical procedure for simulation of unreinforced masonry structures. Comput Struct 2013;120:9–23. https://doi.org/10.1016/j.compstruc.2013.01.012

[26] Rots JG, Invernizzi S. Regularized sequentially linear saw-tooth softening model. Int J Numer Anal Methods Geomech 2004;28(7–8):821–56. https://doi.org/10.1002/NAG.371

[27] Pari M, Van de Graaf AV, Hendriks MAN, Rots JG. A multi-surface interface model for sequentially linear methods to analyse masonry structures. Eng Struct 2021;238:112123. https://doi.org/10.1016/J.ENGSTRUCT.2021.112123

[28] Davis L, Cogliano M, Casotto C, Grecchi G, Ozcebe S, Tsioli C, Malomo D, et al. Pragmatic seismic collapse meso-scale analysis of old Dutch masonry churches. Earthq Eng Struct Dyn 2023;53:622–45. https://doi.org/10.1002/EQE.4037

[29] Kassotakis N, Sarhosis V, Riveiro B, Conde B, D'Altri AM, Mills J, Milani G, de Miranda S, Castellazzi G, et al. Three-dimensional discrete element modelling of rubble masonry structures from dense point clouds. Autom Constr 2020;119:103365. https://doi.org/10.1016/J.AUTCON.2020.103365

[30] Mendes N, Zanotti S, Lemos JV. Seismic performance of historical buildings based on discrete element method: an Adobe church. J Earthq Eng 2020;24(8):1270–89. https://doi.org/10.1080/13632469.2018.1463879

[31] Schiavoni M, Giordano E, Roscini F, Clementi F. Advanced numerical insights for an effective seismic assessment of historical masonry aggregates. Eng Struct 2023;285:115997. https://doi.org/10.1016/J.ENGSTRUCT.2023.115997

[32] Malomo D, DeJong MJ, Penna A. Distinct element modelling of the in-plane cyclic response of URM walls subjected to shear-compression. Earthq Eng Struct Dyn 2019;48(12):1322–44. https://doi.org/10.1002/eqe.3178

[33] Damiani N, DeJong MJ, Albanesi L, Penna A, Morandi P. Distinct element modeling of the in-plane response of a steel-framed retrofit solution for URM structures. Earthq Eng Struct Dyn 2023;52(10):3030–52. https://doi.org/10.1002/eqe.3910

[34] Pulatsu B, Wilson R, Lemos JV, Mojsilović N. Exploring the cyclic behaviour of URM walls with and without damp-proof course (DPC) membranes through discrete element method. Infrastructures 2024;9(1):11. https://doi.org/10.3390/INFRASTRUCTURES9010011

[35] Cundall PA. Formulation of a three-dimensional distinct element model—part I. A scheme to detect and represent contacts in a system composed of many polyhedral blocks. Int J Rock Mech Min Sci Geomech Abstr 1988;25(3):107–16. https://doi.org/10.1016/0148-9062(88)92293-0

[36] Cundall P, Detournay C. Dynamic relaxation applied to continuum and discontinuum numerical models in geomechanics. Rock Mech Eng 2017:45–90. https://doi.org/10.1201/B20402-2

[37] Belytschko T. An overview of semidiscretization and time integration procedures. In Belytschko T, Hughes T, editors. Computational methods for transient analysis. New York: Elsevier Science Publisher; 1983. p. 1–65.

[38] Smolinski P, Sleith S, Belytschko T. Stability of an explicit multi-time step integration algorithm for linear structural dynamics equations. Comput Mech 1996;18:236–44.

[39] Lemos JV, Bagi K. Discrete element modeling. Cham: Springer Nature Switzerland; 2023. p. 189–232. https://doi.org/10.1007/978-3-031-32476-5_5. ISBN 978-3-031-32476-5. [Chap. 4].

[40] Oktiovan YP, Davis L, Wilson R, Dell'Endice A, Mehrotra A, Pulatsu B, Malomo D, et al. Simplified micro-modeling of a masonry cross-vault for seismic assessment using the distinct element method. Int J Architect Herit 2023. https://doi.org/10.1080/15583058.2023.2277328

[41] Itasca Consulting Group Inc. 3DEC - three dimensional distinct element code Ver. 9.1. Software; 2023.

[42] Jafari S. Material characterisation of existing masonry: a strategy to determine strength, stiffness and toughness properties for structural analysis [Ph.D. thesis]. Delft: Delft University of Technology; 2021. https://doi.org/10.4233/uuid:3bcbbc72-0212-44e9-ac86-2fdc54ec5987

[43] Chaimoon K. Numerical simulation of fracture in unreinforced masonry [Ph.D. thesis]. Sydney: University of New South Wales; 2007. https://doi.org/10.26190/UNSWORKS/17488

[44] Pluijm VDR. Out-of-plane bending of masonry: behaviour and strength [Ph.D. thesis]. Eindhoven, Netherlands: Technische Universiteit Eindhoven; 1999. https://doi.org/10.6100/IR528212

[45] Li Y, Zeng B. Modeling of masonry structures using a new 3d cohesive interface material model considering dilatancy softening. Eng Struct 2023;277:115466. https://doi.org/10.1016/J.ENGSTRUCT.2022.115466

[46] van Zijl G. Modeling masonry shear-compression: role of dilatancy highlighted. J Eng Mech 2004;130(11):1289–96. https://doi.org/10.1061/(asce)0733-9399(2004)130:11(1289)

[47] Giambanco G, Rizzo S, Spallino R. Numerical analysis of masonry structures via interface models. Comput Methods Appl Mech Eng 2001;190(49–50):6493–511. https://doi.org/10.1016/S0045-7825(01)00225-0

[48] Sharma S, Graziotti F, Magenes G. Torsional shear strength of unreinforced brick masonry bed joints. Constr Build Mater 2021;275:122053. https://doi.org/10.1016/J.CONBUILDMAT.2020.122053

[49] Oliveira DV, Lourenço PB. Implementation and validation of a constitutive model for the cyclic behaviour of interface elements. Comput Struct 2004;82(17–19):1451–61. https://doi.org/10.1016/J.COMPSTRUC.2004.03.041

[50] Atkinson RH, Amadei BP, Saeb S, Sture S. Response of masonry bed joints in direct shear. J Struct Eng 1989;115(9):2276–96. https://doi.org/10.1061/(ASCE)0733-9445(1989)115:9(2276). https://ascelibrary.org/doi/abs/10.1061/.

[51] Facconi L, Minelli F, Vecchio FJ. Predicting uniaxial cyclic compressive behavior of brick masonry: new analytical model. J Struct Eng 2018;144(2). https://doi.org/10.1061/(asce)st.1943-541x.0001961

[52] Ispir M, Ilki A. Behavior of historical unreinforced brick masonry walls under monotonic and cyclic compression. Arab J Sci Eng 2013;38(8):1993–2007. https://doi.org/10.1007/S13369-013-0567-4/METRICS. https://link.springer.com/article/10.1007/s13369-013-0567-4.

[53] Naraine K, Sinha S. Cyclic behavior of brick masonry under biaxial compression. J Struct Eng 1991;117(5):1336–55. https://doi.org/10.1061/(ASCE)0733-9445(1991)117:5(1336). https://ascelibrary.org/doi/abs/10.1061/.

[54] Mojsilović N. Masonry subjected to semi-cyclic compression: inelastic response modelling. Constr Build Mater 2020;263:120147. https://doi.org/10.1016/J.CONBUILDMAT.2020.120147

[55] Segura J, Pelà L, Roca P. Monotonic and cyclic testing of clay brick and lime mortar masonry in compression. Constr Build Mater 2018;193:453–66. https://doi.org/10.1016/J.CONBUILDMAT.2018.10.198

[56] Crisafulli FJ. Seismic behaviour of reinforced concrete structures with masonry infills [Ph.D. thesis]. Christchurch, New Zealand: University of Canterbury, Civil Engineering; 1997. https://doi.org/10.26021/1979

[57] Mander JB, Priestley MJN, Park R. Theoretical stress-strain model for confined concrete. J Struct Eng 1988;114(8):1804–26. https://doi.org/10.1061/(ASCE)0733-9445(1988)114:8(1804). https://ascelibrary.org/doi/abs/10.1061/.

[58] Eibl J, Keintzel E, Vratsanouu V. Determination of earthquake duration dependent behaviour factors for unreinforced brick masonry panels by nonlinear time history calculations. In: Proc. 11th world conf. On earthquake engineering. Amsterdam, Netherlands: Elsevier; 1996. p. 1–8.

[59] Naraine K, Sinha S. Loading and unloading stress-strain curves for brick masonry. J Struct Eng 1989;115(10):2631–44. https://doi.org/10.1061/(ASCE)0733-9445(1989)115:10(2631). https://ascelibrary.org/doi/abs/10.1061/.

[60] Galman I. ściany z ceramicznej cegły pełnej cyklicznie ściskane w swej płaszczyźnie lub zginane prostopadle do płaszczyzny [Ph.D. thesis]. Gliwice, Poland: Silesian University of Technology; 2012. In Polish.

[61] Lee J, Bong HJ, Lee MG. Return mapping with a line search method for integrating stress of the distortional hardening law with differential softening. Comput Struct 2021;257:106652. https://doi.org/10.1016/J.COMPSTRUC.2021.106652

[62] Esposito R, Messali F, Rots JG. Tests for the characterization of replicated masonry and wall ties. Report; 2016. http://resolver.tudelft.nl/uuid:a0923cf9-0ccd-48a1-9ce1-082aa66e97af.

[63] Jafari S, Rots JG, Esposito R. A correlation study to support material characterisation of typical Dutch masonry structures. J Build Eng 2022;45. https://doi.org/10.1016/j.jobe.2021.103450

[64] Comité Euro-International du Béton (CEB). CEB-FIP model code 1990. Lausanne, Switzerland: Thomas Telford; 1993. Bulletin d'information No. 213/214.

[65] Messali F, Esposito R, Ravenshorst GJP, Rots JG. Experimental investigation of the in-plane cyclic behaviour of calcium silicate brick masonry walls. Bull Earthq Eng 2020;18(8):3963–94. https://doi.org/10.1007/s10518-020-00835-x

[66] Sousamli M. Orthotropic cyclic continuum constitutive model for masonry structures and comparative studies [Dissertation]. Delft, The Netherlands: Delft University of Technology; 2024.